

## Observing Surf-Zone Dispersion with Drifters

MATTHEW SPYDELL, FALK FEDDERSEN, AND R. T. GUZA

*Integrative Oceanography Division, Scripps Institution of Oceanography, La Jolla, California*

W. E. SCHMIDT

*Center for Coastal Hazards, Department of Marine Sciences, University of Puerto Rico, Mayagüez, Puerto Rico*

(Manuscript received 3 March 2006, in final form 5 March 2007)

### ABSTRACT

Surf-zone dispersion is studied using drifter observations collected within about 200 m of the shoreline (at depths of less than about 5 m) on a beach with approximately alongshore uniform bathymetry and waves. There were about 70 individual drifter releases, each 10–20 min in duration, on two consecutive days. On the first day, the sea-swell significant wave height  $H_s$  was equal to 0.5 m and mean alongshore currents  $|\bar{v}|$  were moderate ( $<0.1 \text{ m s}^{-1}$ ). On the second day, the obliquely incident waves were larger, with  $H_s$  equal to 1.4 m, and at some surf-zone locations  $|\bar{v}|$  was greater than  $0.5 \text{ m s}^{-1}$ . The one-particle diffusivity was larger, with larger waves and stronger currents. On both days, the one-particle diffusivity tensor is nonisotropic and time-dependent. The major axis is initially parallel to the cross-shore direction, but after a few wave periods it is aligned with the alongshore direction. In both the along- and cross-shore directions, the asymptotic diffusivity is reached sooner within, rather than seaward of, the surf zone. Two-particle statistics indicate that relative dispersion grows like  $D^2(t) \sim t^{3/2}$  and that the relative diffusivity is scale-dependent as  $\mu \sim l^{2/3}$ , with  $l$  being the particle separation. The observed scalings differ from 2D inertial-subrange scalings [ $D^2(t) \sim t^3$  and  $\mu \sim l^{4/3}$ ]. Separations have a non-Gaussian self-similar distribution that is independent of time. The two-particle statistics are consistent with a nonconstant-coefficient diffusion equation for the separation probability density functions. The dispersion is explained by neither irrotational surface gravity waves nor shear dispersion. The observations imply the existence of a 2D eddy field with 5–50-m length scales, the source of which is speculated to be alongshore gradients in breaking-wave height associated with finite crest lengths.

### 1. Introduction

Beaches are a significant piston in the economic engine of urban coastal regions. Terrestrial runoff pollution dominates urban pollutant loading rates (Schiff et al. 2000). Runoff pollution often drains directly onto the shoreline. Upon entering ocean waters, the runoff is first mixed, dispersed, and advected within the surf zone. Runoff pollution degrades water quality in the surf zone and leads to beach closures (e.g., Boehm et al. 2002). It increases the health risks (e.g., diarrhea and upper respiratory illness) to ocean bathers (Haile et al. 1999) and contains both human viruses (Jiang and Chu 2004) and elevated levels of fecal bacteria (Reeves et al.

2004). Given a source, the transport direction (up- or downcoast) in the surf zone can be correctly predicted (e.g., Ruessink et al. 2001; Grant et al. 2005) from the incoming wave field and the wind. However, the details of pollution dispersal in nearshore and surf-zone environments are not well understood.

A useful measure of dispersion, the “eddy” diffusivity, parameterizes the bulk dispersal effects of the turbulent velocities on the mean concentration. To be specific, horizontal tracer dispersion is modeled by the two-dimensional (2D) integro-differential advection diffusion equation

$$\partial_t \Theta + \mathbf{U} \cdot \nabla \Theta = \nabla \cdot \int_0^t \partial_{t'} \kappa(t') \cdot \nabla \Theta(t - t') dt', \quad (1)$$

where  $\kappa$  is the eddy diffusivity tensor,  $\mathbf{U}$  is the (depth averaged) mean horizontal velocity,  $\Theta$  is the (ensemble

*Corresponding author address:* M. Spydell, Scripps Institution of Oceanography, 9500 Gilman Dr., La Jolla, CA 92093-0209.  
E-mail: mspydell@ucsd.edu

averaged) mean concentration field (Davis 1987), and  $\kappa$ ,  $\mathbf{U}$ , and  $\Theta$  depend on position and time. For time-independent  $\kappa$ , the right-hand side of (1) is  $\nabla \cdot \kappa \nabla \Theta$ , recovering the familiar advection–diffusion equation. There are two kinds of eddy diffusivities: absolute ( $\kappa$ ) and relative ( $\mu$ ). Absolute diffusivities characterize tracer dispersion averaged over many releases in a coordinate frame fixed to the common release point. Relative diffusivities describe the spreading of the average cloud in a coordinate frame fixed to each individual cloud’s center of mass, and so the spatial coordinates in the diffusion equation refer to cloud size or separation (Richardson 1926).

Few previous studies have examined dispersion in the nearshore, and eddy diffusivity estimates vary considerably. Based on observed dye dilution, Inman et al. (1971) obtained cross-shore diffusivities  $\kappa_{xx}$  that are between 0.08 and 5.9  $\text{m}^2 \text{s}^{-1}$  and alongshore  $\kappa_{yy}$  that are between 0.03 and 0.17  $\text{m}^2 \text{s}^{-1}$ . For three separate beaches, Clarke et al. (2007) fit time series of shoreline dye concentration at different alongshore locations to diffusion models of varying complexity. The diffusivity estimates varied widely [ $\kappa$  from  $O(10^{-1})$  to  $O(10^2) \text{m}^2 \text{s}^{-1}$ ] depending on the wave and circulation conditions and, in particular, the presence of rip currents. Grant et al. (2005) measured dye spreading rates, with considerably longer experiment duration  $O(10^3) \text{s}$ , and estimated  $40 < \mu_{yy} < 80 \text{m}^2 \text{s}^{-1}$ , where larger values correspond to larger waves.

Dispersion can also be estimated from Lagrangian drifter data and is equivalent to observing tracer dispersion. Theories for one-particle (absolute) diffusivities in spatially homogeneous (Taylor 1921) and inhomogeneous (Davis 1987) flows have been developed. Two-particle (relative) dispersion has been extensively studied—in particular in stationary, homogeneous turbulence. Using atmospheric observations, Richardson (1926) found a separation ( $l$ )-dependent (or scale dependent) relative diffusivity  $\mu \sim l^{4/3}$  (e.g., Richardson’s law). This scale-dependent  $\mu$  has been observed in some geophysical flows (Okubo 1971; LaCasce and Bower 2000).

Surface (and subsurface) drifters have been used to estimate directly the large-scale  $\kappa$  of the general circulation (e.g., Lumpkin et al. 2002; Zhurbas and Oh 2003), the California Current (Swenson and Niiler 1996), and continental-shelf regions (Davis 1985; Dever et al. 1998). Using drifters to estimate the spreading rate of multiparticles in rip current–dominated surf-zone circulations, Johnson and Pattiaratchi (2004) estimated  $\mu$  to be between 1.3 and 3.9  $\text{m}^2 \text{s}^{-1}$  and found support for a Richardson-like scale-dependent  $\mu$ . They

also found alongshore relative diffusivities that were larger than cross-shore ones, contrary to dye-release experiments (Inman et al. 1971).

Here, dispersion within about 200 m of the shoreline of a sandy beach (depths of less than 5 m) is characterized using drifter observations acquired on two consecutive days with contrasting waves and currents (section 2). One-particle diffusivities  $\kappa$  are larger on the day with larger waves, and on both days  $\kappa$  is time-dependent, with the alongshore diffusivity usually greater than the cross-shore one (section 3). Two-particle statistics (section 4) indicate a scale-dependent relative diffusivity  $\mu \sim l^{2/3}$  that is weaker than the Richardson scaling  $\mu \sim l^{4/3}$ . The two-particle dispersion does not have the time dependence expected for inertial-subrange turbulence. However, the two-particle statistics are consistent with a diffusion equation for the probability density function (pdf) of particle-pair separations in which the diffusivity depends on both separation and time. The scale-dependent diffusivity suggests the presence of an energetic eddy field with 5–50-m length scales (smaller and larger scales were not studied). In section 5, the present surf-zone diffusivities are compared with other estimates and possible mechanisms for dispersion are discussed. Conclusions follow in section 6.

## 2. Observations

Observations were acquired on 3 November (denoted day 1) and 4 November (day 2) 2004 at a sandy beach in San Diego, California. These days were chosen because of both the small tidal excursions (increasing stationarity) and good GPS satellite coverage. The cross- and alongshore coordinates are  $x$  and  $y$ , with the shoreline at  $x = 0$  and  $x$  increasing negatively offshore. At this location, the bathymetry is nearly uniform alongshore, with slopes of 0.025 offshore of  $x \approx -100 \text{m}$  and 0.015 nearer the shore (Fig. 1). Three Sontek Triton acoustic Doppler velocimeters (ADV), sampling at 2 Hz, were deployed on a cross-shore transect (symbols in Fig. 1b) with sensing volumes 0.8 m above the bed.

Drifter deployments on each day began at 1000 Pacific standard time (PST) and lasted 5–6 h. Tidal changes in sea level were small (about 0.2 and 0.1 m on days 1 and 2, respectively). The wave field and mean currents were roughly stationary (Fig. 2). On day 1, the significant wave height was  $H_s = 0.5 \text{m}$  at the most offshore ADV (Fig. 2b) with a mean period around 9 s. The inner, shallowest ADV was located near the seaward edge of the (visually observed) surf zone. Wind speeds were generally 2–4  $\text{m s}^{-1}$  out of the southwest. Waves were approximately normally incident, resulting

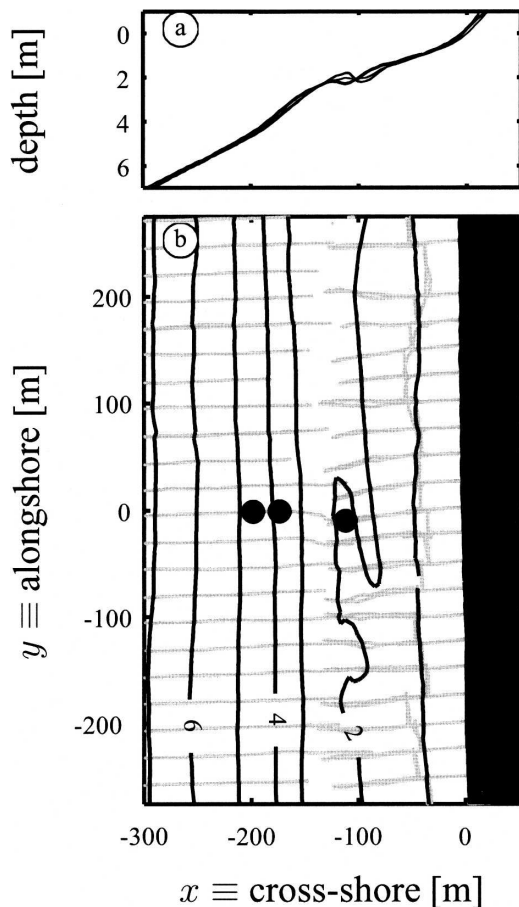


FIG. 1. The nearshore bathymetry (relative to average tide level): (a) depth vs cross-shore position  $x$  at alongshore location  $y = -150, 0,$  and  $150$  m (thick to thin lines) and (b) bathymetry contours at 1-m intervals. Solid black circles indicate ADV locations, and gray lines are survey tracks. The beach was surveyed on 1 Nov 2004.

in weak mean alongshore currents ( $|\bar{v}| < 0.1 \text{ m s}^{-1}$ ). On day 2, waves were larger and obliquely incident. Seaward of the surf zone at the deepest ADV  $H_s = 1.4$  m, whereas wave breaking reduced  $H_s$  to 0.5 m at the shallowest ADV (Fig. 2b). The mean wave period was about 8 s, and winds were about  $4 \text{ m s}^{-1}$  from the northwest. Offshore of the surf zone,  $\bar{v} \approx -0.2 \text{ m s}^{-1}$  (dashed and dashed-dotted in Fig. 2d). The larger, obliquely incident waves drove a strong  $\bar{v}$  in the surf zone at the shallowest ADV (solid in Fig. 2d). Day 2 root-mean-square (rms) velocity fluctuations were about  $0.5 \text{ m s}^{-1}$ , as compared with about  $0.25 \text{ m s}^{-1}$  on day 1 (Figs. 2e,f). The different wave and circulation conditions on the two days provide contrasting conditions for studying surf-zone dispersion.

The freely floating, impact-resistant, GPS-tracked surf-zone drifters are 0.5-m-tall cylinders with most of

their volume below the water line. A horizontal disc at the bottom of the body tube dampens vertical motions in the waves, allowing broken waves to pass over the drifter without pushing or “surfing” it ashore. Drifter wind slip is 1% of the wind speed (Schmidt et al. 2003)—a few centimeters per second in the conditions discussed here. Eulerian (from the ADVs) and Lagrangian (from drifter) cross-shore velocity spectra are similar in the sea-swell band on both days, as also found by Schmidt et al. (2003). In addition, mean alongshore currents derived from drifter trajectories agree well with fixed current meters (Schmidt et al. 2003), and observed drifter trajectories are roughly consistent with trajectories predicted by a numerical nearshore circulation model (Schmidt et al. 2005).

Drifter GPS positions are internally recorded at 1 Hz with absolute position error of about  $\pm 4$  m (George and Largier 1996). Postprocessing using carrier-phase information reduces the absolute error to  $\pm 1$  m (Doutt et al. 1998). Gaps in the time series of drifter positions occur when waves pass over the drifter, interrupting the satellite communication. Gaps in  $\pm 1$ -m positions are more common because the higher accuracy requires 16 s of continuous satellite communication. Continuous time series of drifter positions were obtained by filling gaps in the  $\pm 1$ -m time series with  $\pm 4$ -m positions. Gaps in the  $\pm 4$ -m series are filled using spline interpolation if the gap is smaller than 10 s and linear interpolation if the gap is larger than 10 s. On day 1, more than 70% of the position data have  $\pm 1$ -m accuracy, and most of the remaining points have  $\pm 4$ -m accuracy. The larger waves of day 2 result in increased gaps; however, only 6% of the data points were in gaps longer than 10 s. Last, the time series are smoothed with a 7-point Gaussian filter with an  $e$ -folding time of 2 s.

All nine drifters were released simultaneously on a cross-shore transect (Fig. 3). Two drifters were released side by side at each of four cross-shore locations, and a single drifter was released at a fifth location. The cross-shore transects spanned 70 m on day 1 and 130 m on day 2 (open circles in Figs. 3a,b). The day-2 drifter release locations were scattered (Fig. 3b) because of the large waves and strong alongshore current (Figs. 2b,d). After each release, the drifters floated freely for between 10 and 20 min until they either left the study region ( $y < -120$  m) or were grounded, and then they were collected. After retrieval, all drifters were simultaneously released again on the same cross-shore transect. There were nine (eight) transectwide releases on day 1 (2), yielding 77 (68) usable individual trajectories.

Mean and fluctuating Eulerian currents, over roughly

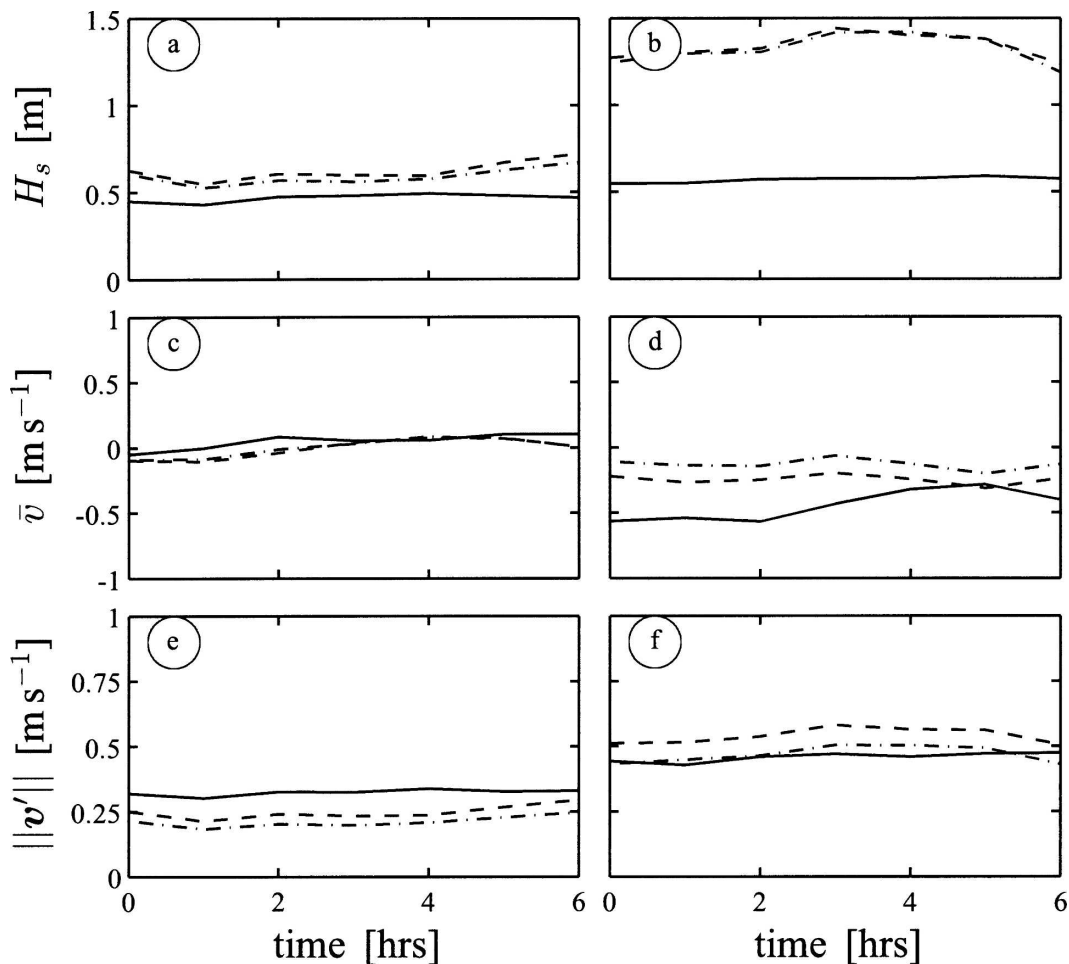


FIG. 2. Time series on (left) day 1 (3 Nov) and (right) day 2 (4 Nov) of hourly (a), (b) significant wave height  $H_s$ , (c), (d) mean alongshore current  $\bar{v}$ , and (e), (f) rms velocity fluctuation  $\|v'\| = ((u'^2) + (v'^2))^{1/2}$ , where  $\langle u'^2 \rangle$  and  $\langle v'^2 \rangle$  are cross- and alongshore velocity variances, over all frequencies. The curves represent the shallowest (solid), middle (dashed), and deepest (dashed-dotted) ADVs. The start time on each day was 1000 PST.

200 m in the cross-shore direction and 250 m in the alongshore direction, were determined from drifter trajectories (Fig. 4). Eulerian mean currents were weaker on day 1 than on day 2 (Figs. 4a,c), as observed with the ADVs (Figs. 2c,d). On day 1, the maximum mean alongshore current is approximately  $0.2 \text{ m s}^{-1}$  close to the shoreline, and on day 2 it is southward and  $\sim 0.7 \text{ m s}^{-1}$  near the approximate “breakpoint” location  $x_b$  (determined visually as  $x_b = -90 \text{ m}$  on day 1 and  $-130 \text{ m}$  on day 2). The day-2 cross-shore shear  $\partial\bar{v}/\partial x$  is  $O(10^{-2}) \text{ s}^{-1}$ , possibly generating shear waves. The maximum drifter-based fluctuating currents  $\|v'\|_{\max}$  (see Fig. 2 caption for definition) are also smaller on day 1 than on day 2 ( $0.29$  and  $0.74 \text{ m s}^{-1}$ , respectively). Although a few drifters on day 1 moved offshore (see tracks in Fig. 3a), the observations show that long-lived rip currents did not occur in the study area on either day. The ef-

fective number of degrees of freedom  $N_e$  (appendix A) is approximated as the duration of observations divided by a typical Lagrangian velocity decorrelation time (roughly 40 and 16 s on days 1 and 2, respectively; Figs. 4b,d). On day 1, weak mean currents result in many observations ( $N$  in Fig. 4b) near the release locations (gray dots in Fig. 4b). On day 2, the observations are more uniformly distributed.

### 3. One-particle diffusivity

One-particle statistics describe how the average (over many releases) tracer evolves from a common release point. Albert Einstein in his 1905 doctoral dissertation first established the equivalence of random molecular motions with bulk molecular diffusion (Einstein 1956). These ideas were subsequently applied to trajectories of particles in a spatially homogeneous tur-

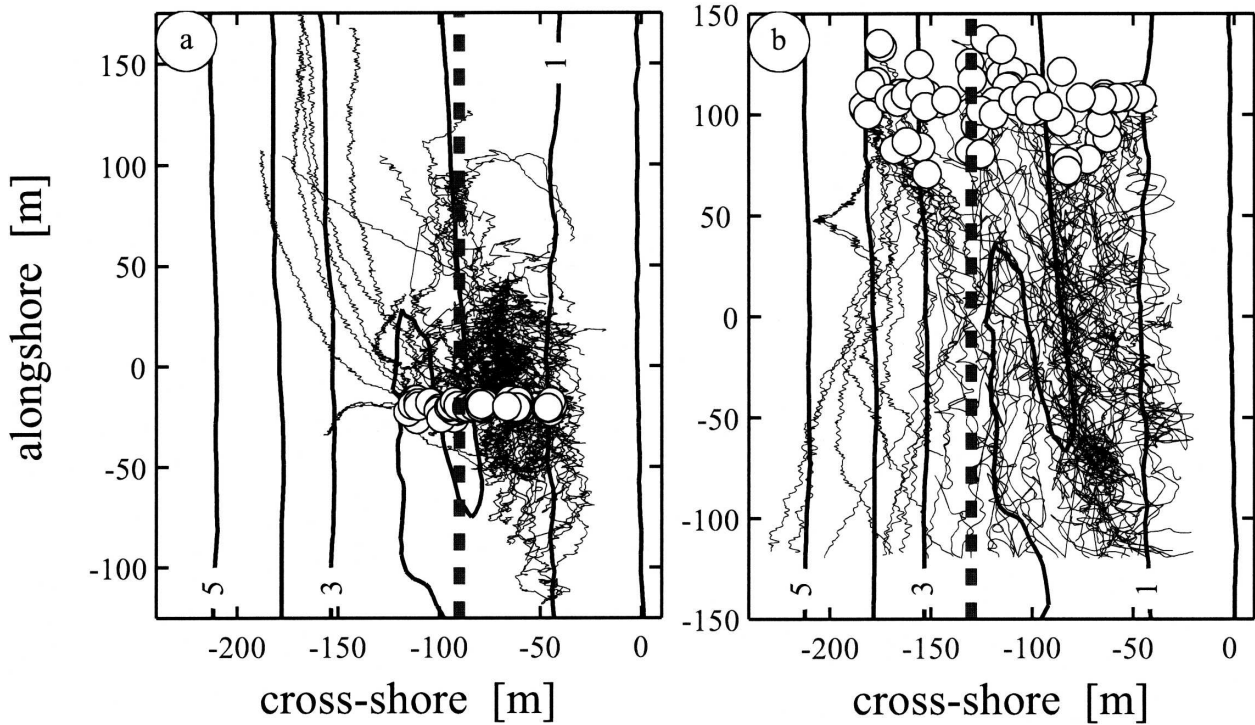


FIG. 3. Drifter tracks for (a) day 1 and (b) day 2 superimposed upon the bathymetry (depth; m). The open circles denote drifter release locations, and the thick dashed line indicates the approximate breakpoint location  $x_b$ . Note the slightly different alongshore scales in (a) and (b).

bulent velocity field (Taylor 1921), relating the one-particle diffusivity  $\kappa_{ij}$  to the time-derivative of displacement variance

$$\kappa_{ij}(t) = \frac{1}{2} \frac{d}{dt} \sigma_{ij}^2(t), \quad (2)$$

where  $\sigma_{ij}^2$  is variance of particle displacements, that is, the second moment of displacements

$$\sigma_{ij}^2(t) = \iint r'_i r'_j C(r'_1, r'_2; t) dr'_1 dr'_2, \quad (3)$$

where  $C(r'_1, r'_2; t)$  is the pdf of a particle displacing  $\mathbf{r}'$  ( $r'_1$ : cross-shore displacement;  $r'_2$ : alongshore displacement) in  $t$  seconds from its starting position and with the mean displacement removed. Assuming spatially homogeneous statistics,  $C(r'_1, r'_2; t)$  is calculated from relative displacements  $\mathbf{r}(t) = \mathbf{x}(t_0 + t) - \mathbf{x}(t_0)$ , with  $\mathbf{x}(t)$  being the position ( $x, y$ ) of a drifter at time  $t$ . Relative displacements are obtained for all  $t_0$ , so that a 100-s time series of positions (for one drifter) sampled at 1 Hz yields 99 rs (1 s), 98 rs (2 s), and so on. Thus, many values of  $\mathbf{r}(t)$  (at short times) are obtained from a single drifter release, and there are about 70 individual releases per day. Anomalous relative displacements are calculated using  $\mathbf{r}'(t) = \mathbf{r}(t) - \mathbf{R}(t)$ , where  $\mathbf{R}(t)$  is the

mean of  $\mathbf{r}(t)$  over all  $t_0$  and drifters. The pdf of anomalous displacements  $C(r'_1, r'_2; t)$  is equivalent to the ensemble average evolution of an initial point source of tracer.

The evolution of  $C(r'_1, r'_2; t)$  on day 1 is shown in Fig. 5. For  $t \leq 25$  s, the pdf is slightly polarized in the cross-shore direction  $r'_1$  (Figs. 5a,b), and, for  $t > 25$  s, the pdf is polarized in the alongshore direction  $r'_2$  (Fig. 5d). Thus, in the (ensemble) average, an initial point source of dye spreads more quickly in the cross-shore direction, becomes circular when  $t \approx 25$  s, and then elongates in the alongshore direction for  $t > 25$  s. Moreover, for approximately  $t > 25$  s, the alongshore spreading rate is larger than the cross-shore spreading rate; thus  $\kappa_{yy} > \kappa_{xx}$  for these times. The cross-shore diffusivity (and patch size  $\sigma_{xx}$ ) would presumably be larger for a surface scalar (e.g., dye) patch because it would be entrained in, and elongated by, breaking waves, whereas drifters do not surf shoreward. On day 2,  $C(r'_1, r'_2; t)$  is similar but spreads more rapidly (not shown).

With cross-shore-varying velocity statistics (Figs. 4a,c),  $\kappa$  depends on position and (2) requires modification (Davis 1987). The drifter position is appended with a label indicating where it came from; that is,  $\mathbf{r}(t|\mathbf{x})$  is the displacement of a drifter  $t$  seconds after it was at

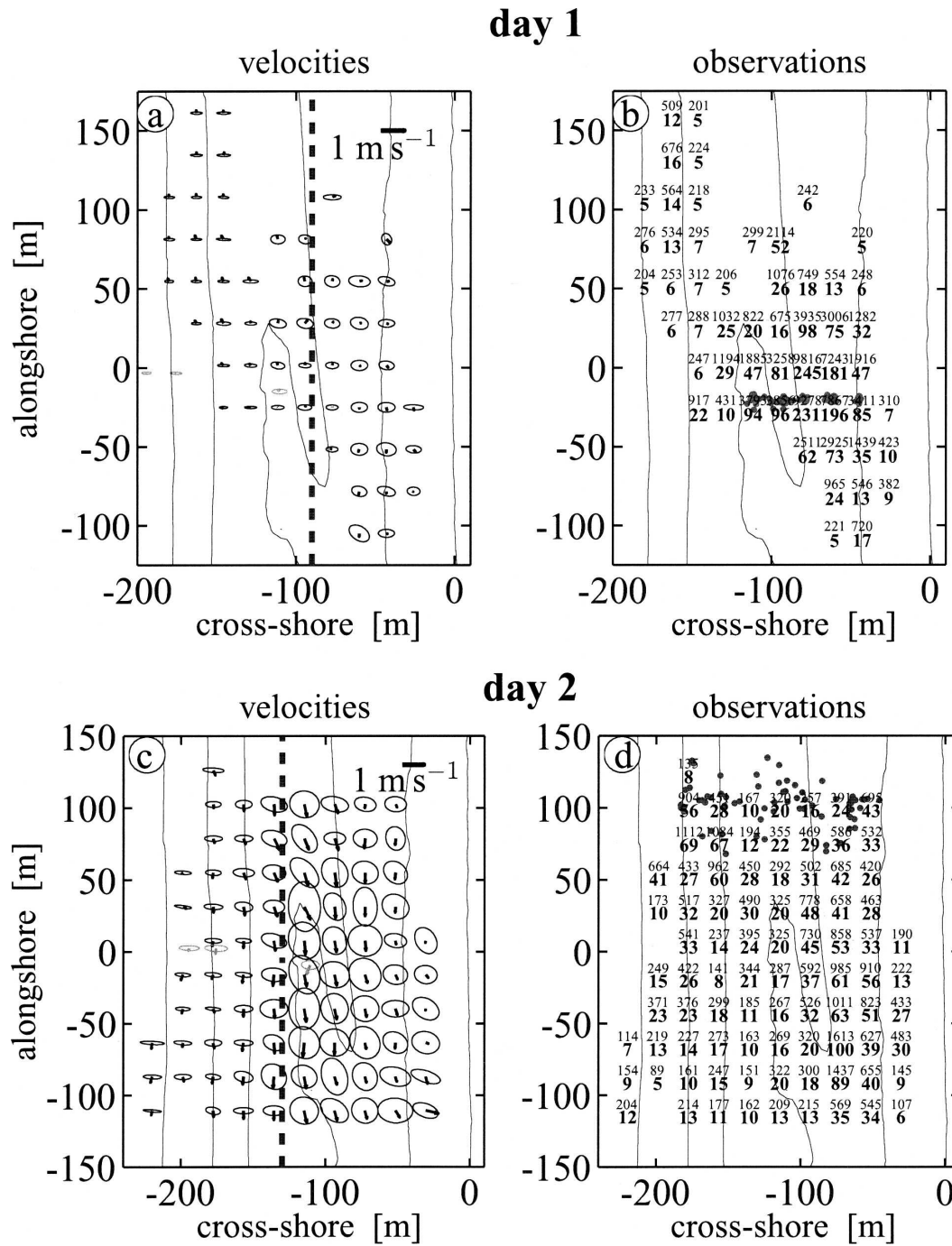


FIG. 4. (a), (c) Plan view of spatially binned mean velocity vector and standard deviation ellipses on (top) day 1 and (bottom) day 2. Scale is indicated in the upper-right corners. ADV-based vectors and ellipses are shown in light gray near  $y = 0$ . Dashed vertical lines indicate the approximate location of  $x_b$ . (b), (d) The corresponding total drifter observation time  $N$  (s; small font) and number of independent observations  $N_e$  (boldface font). Only bins with  $N_e \geq 5$  are shown. Filled small gray circles in (b) and (d) are drifter release locations, and thin lines are depth contours (1-m intervals).

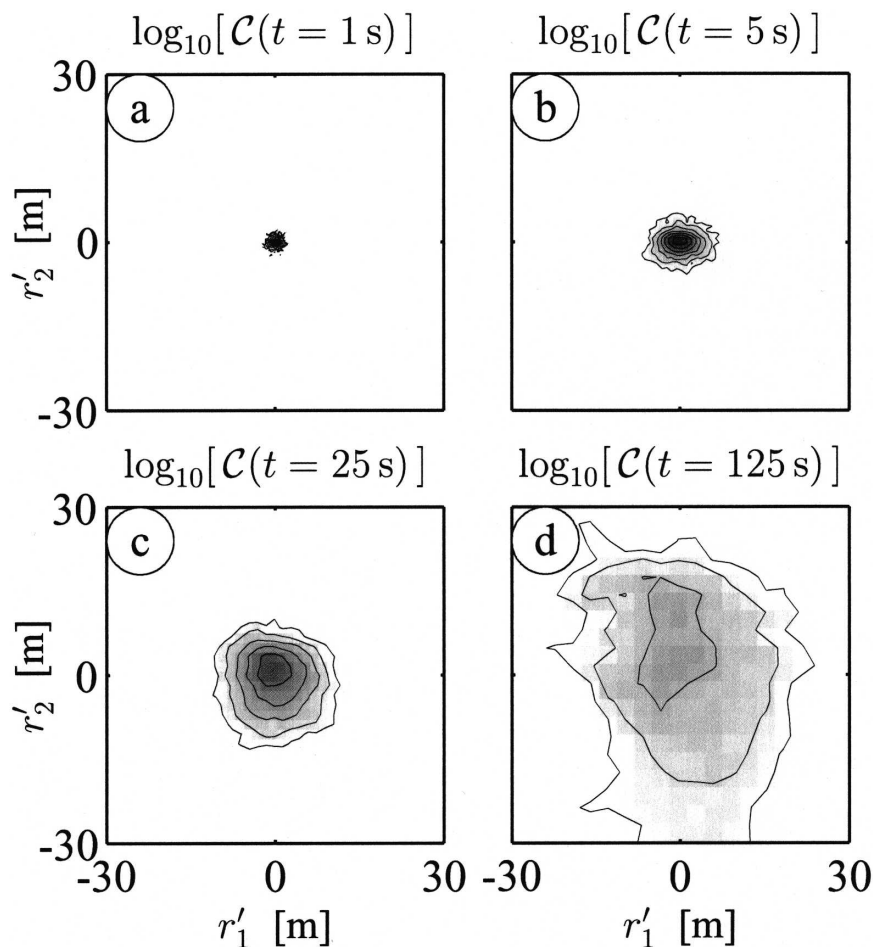


FIG. 5. Contours of the pdf,  $C(r'_1, r'_2; t)$ , of anomalous Lagrangian displacements ( $r'_1$ : cross-shore;  $r'_2$ : alongshore). The contour values displayed are  $\log_{10}[C(r'_1, r'_2; t)] = -4, -3.5, \dots, 0.5$  at times  $t =$  (a) 1, (b) 5, (c) 25, and (d) 125 s.

$\mathbf{x}$ . In a similar way, the drifter velocity is defined as  $\mathbf{v}(t\mathbf{x}) = \partial_t \mathbf{r}(t\mathbf{x})$ . Every drifter that passes through a given spatial bin  $\mathbf{x}$  provides estimates of  $\mathbf{r}(t = 1, 2, 3, \dots | \mathbf{x})$ . Averaging over all drifters that pass through  $\mathbf{x}$  yields a mean drifter trajectory  $\mathbf{R}(t|\mathbf{x})$ , from which a mean Lagrangian drifter velocity is calculated:  $\mathbf{V}(t|\mathbf{x}) = \partial_t \mathbf{R}(t|\mathbf{x})$ . Anomalous Lagrangian drifter velocities,  $v'_i(t|\mathbf{x}) = v_i(t|\mathbf{x}) - V_i(t|\mathbf{x})$ , are used to calculate the spatially dependent anomalous Lagrangian velocity autocovariance,

$$C_{ij}(t, \mathbf{x}) = \langle v'_i(0|\mathbf{x})v'_j(t|\mathbf{x}) \rangle, \quad (4)$$

with angle brackets indicating averaging over all  $t$  time-separated velocities.

With the spatial bin spanning the entire nearshore, the cross-shore velocity covariance  $C_{xx}(t)$  on day 1 shows the presence of surface gravity waves (“ringing” in Fig. 6a) and is much larger than the alongshore ve-

locity covariance  $C_{yy}(t)$  at small  $|t| < 10$  s (Fig. 6b). However,  $C_{yy}(t) > C_{xx}(t)$  for all but small  $|t|$ . The times ( $\tau_{ij}$ ) when  $C_{ij}(t)$  cannot be distinguished from 0 (i.e., is within the sampling error) are  $\tau_{xx} = 150$  s and  $\tau_{yy} = 250$  s. Day 2 results are similar (not shown).

In the method of Davis (1987), the integral of the Lagrangian velocity autocovariance function is the diffusivity

$$\kappa_{ij}(t, \mathbf{x}) = \int_{-t}^0 C_{ij}(t', \mathbf{x}) dt', \quad (5)$$

and  $\kappa(t, \mathbf{x})$  quantifies the spreading rate of  $C(r'_1, r'_2; t, \mathbf{x})$ . The integration is over negative time lags because the diffusivity depends on from where the drifter came rather than on to where it is going. With spatially homogeneous statistics, (2) and (5) are equivalent definitions of  $\kappa$ . However, with spatially inhomogeneous statistics,  $\kappa_{ij}(t, \mathbf{x})$  from (5) is the appropriate diffusivity for use in (1). The diffusivity asymptotically approaches  $\kappa_{ij}^\infty$

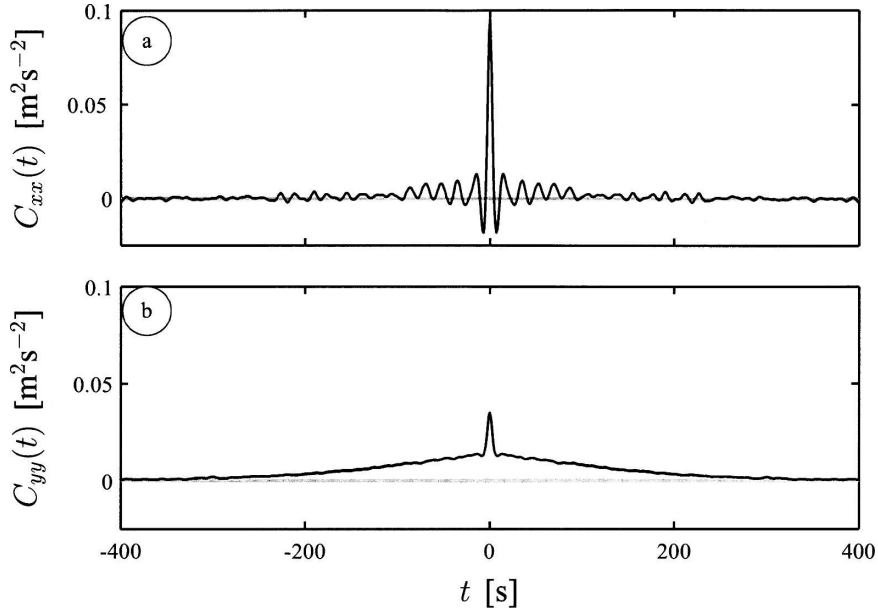


FIG. 6. Day-1 Lagrangian velocity autocovariance functions: (a) cross-shore  $C_{xx}(t)$  and (b) alongshore  $C_{yy}(t)$ . Observations within and seaward of the surf zone are included. Biased (using the number of observations at  $t = 0$  for the number of observations at every  $t$ ) and unbiased estimates of  $C$  lie on each other for the times shown. Values between plus and minus the sampling error [following Bendat and Piersol (2000)] are denoted by the gray area centered at  $C_{ii}(t) = 0$ .

for  $t \geq \tau_{ij}$ , and for these times the right-hand side of (1) becomes  $\nabla \cdot \kappa^\infty \nabla \Theta$  and is independent of time.

Davis (1987) shows that using (5) in (1) is appropriate if the following scale separation is satisfied:

$$\langle r_P^2 \rangle^{1/2} \ll L_Q + \langle \sigma_\tau^2 \rangle^{1/2} \quad \text{and} \quad \langle \sigma_\tau^2 \rangle^{1/2} \ll L_\sigma, \quad (6)$$

where the length scale  $\langle r_P^2 \rangle^{1/2}$  is the maximum predictable displacement knowing the velocity field at a given time,  $L_Q$  is the length scale of the tracer,  $\langle \sigma_\tau^2 \rangle^{1/2}$  is the rms displacement of a particle after  $\tau$  (the time to reach  $\kappa^\infty$ ) seconds, and  $L_\sigma$  is the length scale over which the statistics (of  $\mathbf{v}'$ ) vary (the width of the surf zone; about 50 and 100 m on days 1 and 2, respectively). The other scales are determined after  $\kappa_{ij}$  is calculated. Condition (6) is satisfied on both days.

The one-particle eddy diffusivity  $\kappa_{ij}(t, \mathbf{x})$  is estimated with (5) using the biased (using the number of observations at  $t = 0$  for the number of observations at every  $t$ ) Lagrangian velocity autocovariance function; thus a smooth transition to  $\kappa^\infty$  is ensured. Results are similar but noisier using the unbiased autocovariance function. The relatively small number of drifter releases and the associated statistical uncertainty preclude a high-resolution examination of the spatial ( $x$ ) variation of  $\kappa$ . A  $\kappa$  representative of the entire surf-zone region is first

estimated using all the observations on each day (sections 3a and 3b), and then  $\kappa$  is estimated separately within and seaward of the breaker line (section 3c).

#### a. Results: Day 1

The major axis of diffusion is cross-shore oriented for  $t < 10$  s (cf. Fig. 7a with Fig. 7c), indicating that an ensemble patch initially spreads more quickly cross-shore than alongshore, consistent with previous results (Inman et al. 1971; and others). To be specific, for these times  $\kappa_{xx} - \kappa_{yy} \approx 0.1 \text{ m}^2 \text{ s}^{-1}$ . The major axis of diffusion is alongshore oriented (within  $10^\circ$ ) to the cross-shore direction (Figs. 7b,d) for  $t > 10$  s. After  $(\tau_{xx}, \tau_{yy}) \approx (150, 250)$  s, one-particle diffusivities asymptotically approach  $\kappa_{xx}^\infty \approx 0.65 \text{ m}^2 \text{ s}^{-1}$  and  $\kappa_{yy}^\infty \approx 2 \text{ m}^2 \text{ s}^{-1}$ , respectively. The off-diagonal term of the symmetric diffusivity tensor  $[\kappa_S = (\kappa_{12} + \kappa_{21})/2]$  is small but not negligible (Fig. 7e). At long times,  $\kappa_S^\infty \approx 0.35 \text{ m}^2 \text{ s}^{-1}$  rotates the major axis of diffusion clockwise  $8^\circ$  from the true alongshore direction. Removing the 5 drifters that moved significantly offshore and toward  $+y$  (all during the same release) from the dataset (Fig. 3a) changes the polarization angle by only  $\sim 1^\circ$ , does not significantly alter  $\kappa_{xx}^\infty$ , and decreases  $\kappa_{yy}^\infty$  by 10%.

The ensemble-averaged patch size is obtained using (2):

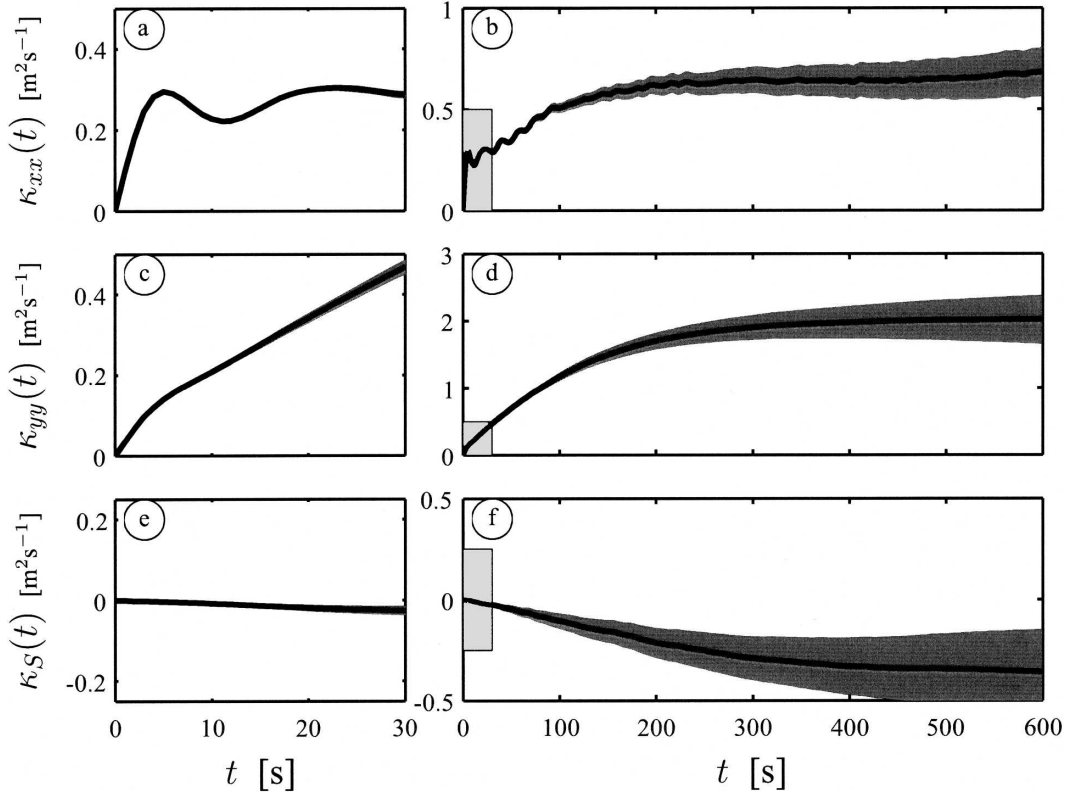


FIG. 7. Day-1 one-particle diffusivities  $\kappa_{ij}(t)$ : (a), (b)  $\kappa_{xx}$ , (c), (d)  $\kappa_{yy}$ , and (e), (f)  $\kappa_S$ , where (a), (c), and (e) are enlargements of the light-gray areas in (b), (d), and (f) and show the initial growth of  $\kappa_{ij}$  with the same vertical scale. The dark-gray shaded region shows values of  $\kappa_{ij}(t) \pm \epsilon_{ij}(t)$ , where  $\epsilon$  is the sampling error (appendix B).

$$\sigma_{ij}(t) = \left[ 2 \int_0^t \kappa_{ij}(t') dt' \right]^{1/2}, \quad (7)$$

where  $\sigma_{xx}$  and  $\sigma_{yy}$  are the cross- and alongshore length scales. The patch becomes circular,  $\sigma_{xx} = \sigma_{yy}$ , at  $t \approx 30$  s and  $\sigma_{xx}/\sigma_{yy} \sim 1.25$  for  $t < 30$  s; after 30 s the patch is elongated in the alongshore direction.

Lagrangian time (i.e., a Lagrangian decorrelation time)  $T_i$  and space scales  $L_i$ , estimated using  $\kappa^\infty$  and the observed velocity variances,

$$T_i = \frac{\kappa_{ii}^\infty}{C_{ii}(t=0)} \quad \text{and} \quad L_i = \frac{\kappa_{ii}^\infty}{\sqrt{C_{ii}(t=0)}}, \quad (8)$$

are  $T_x \sim 7$  s and  $L_x \sim 2$  m and  $T_y \sim 54$  s and  $L_y \sim 10$  m in the cross-shore and alongshore directions, respectively. Note that, at  $t = 0$ ,  $C_{xx}$  is several times as large as  $C_{yy}$  (Fig. 6).

### b. Results: Day 2

On day 2, the incident wave height was almost 3 times as large as and more obliquely incident than on day 1, resulting in larger  $\bar{v}$  and  $\|\mathbf{v}'\|$  (Fig. 2). The more

energetic conditions on day 2 lead to  $\kappa^\infty$  that are between 2 and 3 times as large as on day 1 (cf. Fig. 8 with Fig. 7). For  $t < 20$  s,  $\kappa_{xx} \geq \kappa_{yy}$  (Figs. 8a,c), and  $\kappa_{xx} < \kappa_{yy}$  for  $t > 20$  s. Similar to day 1, for small times ( $t < 30$  s) on day 2 the patch is elongated in the cross-shore direction,  $\sigma_{xx} > \sigma_{yy}$ . The asymptotic values  $\kappa_{xx}^\infty \approx 1.5$   $\text{m}^2 \text{s}^{-1}$  and  $\kappa_{yy}^\infty \approx 4.25$   $\text{m}^2 \text{s}^{-1}$  are reached when  $(\tau_{xx}, \tau_{yy}) \approx (50, 200)$  s. The symmetric term,  $\kappa_S^\infty \approx -0.2$   $\text{m}^2 \text{s}^{-1}$ , rotates the major axis of diffusion clockwise a few degrees from the alongshore axis. The sampling error is larger on day 2 because the average duration of a drifter trajectory was shorter. Day-2 Lagrangian time and length scales ( $T_x = 4.6$  s,  $T_y = 15.0$  s,  $L_x = 2.6$  m, and  $L_y = 8.0$  m) are shorter than on day 1 (section 3a).

### c. Cross-shore dependence

Davis (1987) extended (2) to spatially inhomogeneous velocity fields and obtained (5) to estimate spatially varying  $\kappa_{ij}(t, \mathbf{x})$  from Lagrangian observations. Observations are divided into two regions, within (or “inside”) and seaward (or “outside”) of the surf zone separated by  $x_b$  (dashed gray line in Figs. 4a,c). Velocity

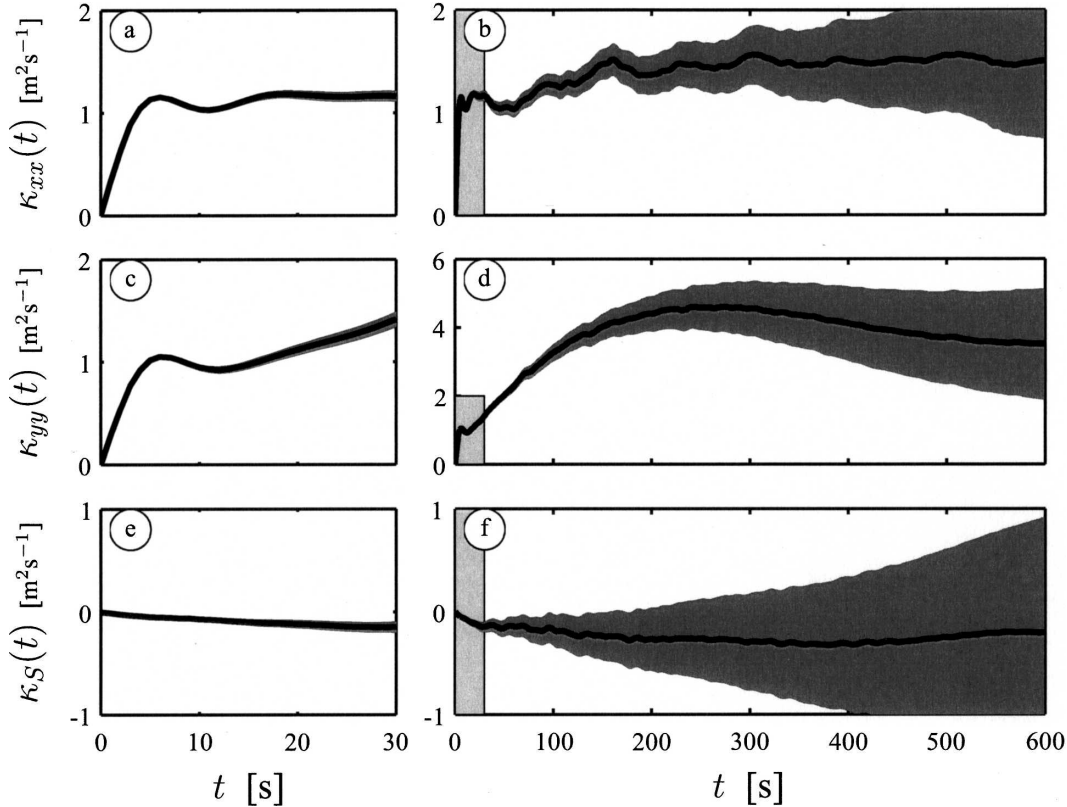


FIG. 8. As in Fig. 7, but for day 2 and with different scales.

fluctuations are larger in the surf zone (Figs. 4a,c). Note that the statistics are still spatially inhomogeneous within each region.

The one-particle diffusivity  $\kappa_{ij}(t, \mathbf{x})$ , estimated using (5) in both regions and on both days, is consistent with  $\boldsymbol{\kappa}$  estimates for the entire region (cf. Fig. 9 with Figs. 7, 8). On both days,  $k_{xx}$  and  $k_{yy}$  rise more rapidly in the surf zone (Figs. 9a,b). On day 2, inside the surf zone  $\kappa_{xx}^\infty$  is reached in under 30 s, whereas outside the surf zone this takes about 200 s. In a similar way, the time to asymptotically approach for  $\kappa_{yy}$  is longer outside the surf zone on both days (Figs. 9c,d). The longer time for  $\kappa_{xx}$  and  $\kappa_{yy}$  to asymptotically approach outside the surf zone indicates that different eddy processes are responsible for the dispersion in each region and suggests that processes associated (directly or indirectly) with wave breaking are responsible for the increased surf-zone dispersion at short time lags. Despite the different time to asymptotically approach,  $\kappa^\infty$  values (on each day) inside and outside the surf zone are nearly the same, possibly because of the method of calculating  $\boldsymbol{\kappa}(t, \mathbf{x})$ . For large enough times, a drifter originally outside the surf zone may also sample inside the surf zone and vice versa. Inside the surf zone,  $\kappa_S$  has smaller magnitude than outside the surf zone (Figs. 9e,f). Outside the surf

zone, the sign of  $\kappa_S$  changes from day 1 to day 2, changing (rotating) the principle axes of diffusion. This rotation could be due to poor sampling but is also roughly consistent with changes in the incoming swell direction.

Gradients in the antisymmetric term,  $\kappa_A = (\kappa_{12} - \kappa_{21})/2$ , of the diffusivity tensor can advect a tracer patch. For time-independent  $\boldsymbol{\kappa}$ , the advection diffusion equation in (1) can be written as

$$\partial_t \Theta + (U_i + \tilde{U}_i) \partial_i \Theta = \partial_i (\kappa_{ij}^S \partial_j \Theta), \quad (9)$$

where  $\tilde{\mathbf{U}} = \partial_y \kappa_A \mathbf{i} - \partial_x \kappa_A \mathbf{j}$  is the tracer advection resulting from gradients in the antisymmetric part  $\kappa_A$  of the diffusivity tensor. This advection is known as the skew flux or the residual circulation (e.g., Plumb 1979; Ferrari and Plumb 2003) and is analogous to a Stokes drift.

Because only cross-shore gradients of  $\kappa_A$  are calculated, only the alongshore skew flux ( $-\partial_x \kappa_A$ ) is examined. The cross-shore gradient in  $\kappa_A$  (Figs. 9g,h) corresponds to weak alongshore advection of about 0.01 and  $-0.02 \text{ m s}^{-1}$  on days 1 and 2, respectively. Thus, on average, a tracer patch will advect slightly (and on day 2 with the mean alongshore current) because of this skew-flux mechanism. On both days, the  $\kappa_A$  gradient only becomes significant at time lags greater than 100 s,

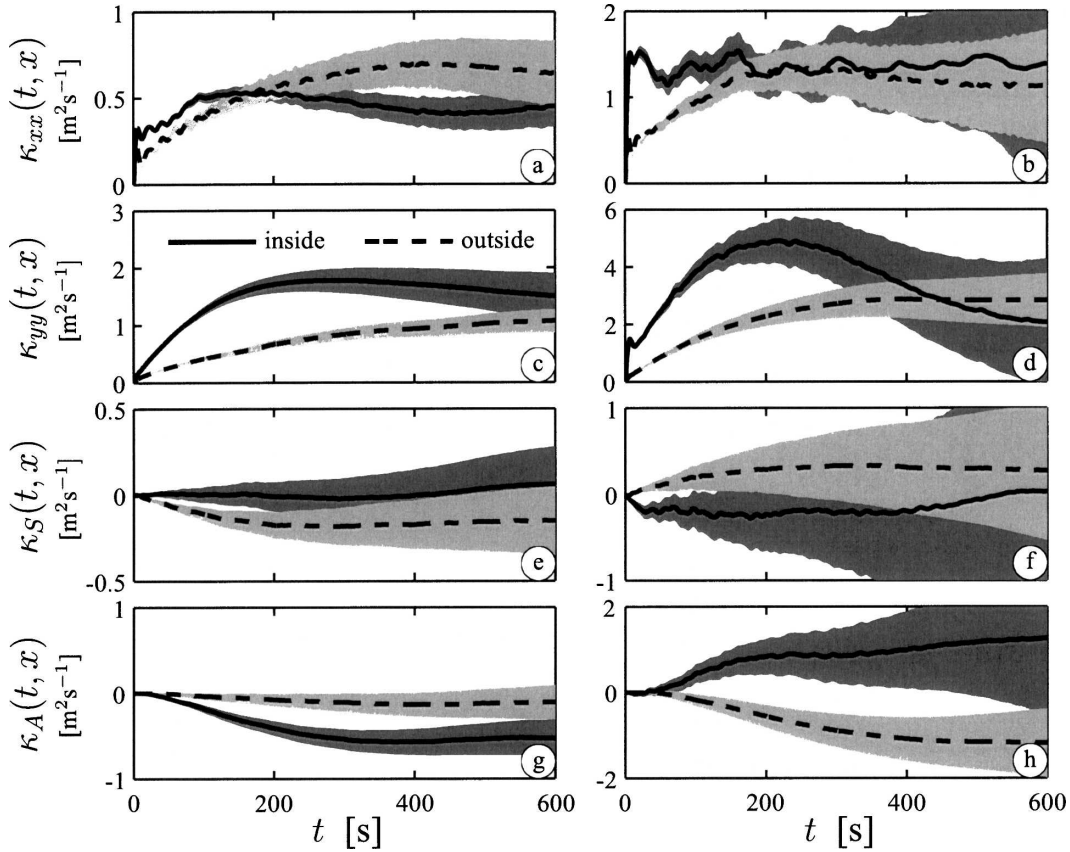


FIG. 9. One-particle eddy diffusivities (top to bottom)  $\kappa_{xx}$ ,  $\kappa_{yy}$ ,  $\kappa_S$ , and  $\kappa_A$  for (left) day 1 and (right) day 2. Results are shown within ( $x > x_b$ ; solid) and seaward ( $x < x_b$ ; dashed) of the surf zone. The scale for day 2 is 2 times that for day 1 for each component of the diffusivity tensor. The sampling error is indicated by the shaded regions (appendix B).

much longer than a wave period, indicating that the eddy processes responsible for the skew-flux are not surface gravity wave-related.

#### 4. Two-particle statistics

Two-particle statistics describe the evolution of the average cloud in a coordinate frame fixed to the center of mass of each individual cloud. The probability density function of two-particle separations (angle brackets denote expectation) is

$$P_s(\mathbf{s}, t, \mathbf{s}_0) = \langle \delta[\mathbf{s} - \mathbf{y}(t, \mathbf{s}_0)] \rangle, \quad (10)$$

where  $\mathbf{s}$  is a separation vector between two particles and  $\mathbf{y}(t, \mathbf{s}_0)$  is the two-particle separation at time  $t$  with separation  $\mathbf{s}_0$  at  $t = 0$ ; thus  $\mathbf{y}(t = 0, \mathbf{s}_0) = \mathbf{s}_0$ . The second moment of  $P_s$ , the “relative dispersion,” is

$$D_{ij}^2(t, \mathbf{s}_0) = \int \int s'_i s'_j P_s(\mathbf{s}' + \mathbf{s}_0, t, \mathbf{s}_0) ds'_1 ds'_2, \quad (11)$$

where  $\mathbf{s}' = \mathbf{s} - \mathbf{s}_0$ . The mean separation is assumed to be equal to  $\mathbf{s}_0$  for all  $t$ . The “cloud size” in the  $i$ th direction  $l_i$  is given by

$$l_i^2(t) = D_{ii}^2(t, \mathbf{s}_0) + s_{0i}^2, \quad (12)$$

and the time derivative of  $D^2$  is the relative (two particle) diffusivity

$$\mu_{ij}(t, \mathbf{s}_0) = \frac{1}{4} \frac{d}{dt} D_{ij}^2(t, \mathbf{s}_0). \quad (13)$$

The  $1/4$  provides equivalence between the relative and absolute diffusivities in the limit

$$\mu_{ij}^\infty \rightarrow \kappa_{ij}^\infty \quad \text{for } t \gg T_{\max}(|\mathbf{s}_0|) \quad \text{or } |\mathbf{s}_0| \gg L_{\max}, \quad (14)$$

where  $L_{\max}$  is the longest length scale in the flow and  $T_{\max}(|\mathbf{s}_0|)$  is the time for two particles initially separated by  $|\mathbf{s}_0|$  to reach an  $L_{\max}$  separation. Thus, when sufficiently separated, particles move independently and the relative dispersion is the sum of individual one-particle dispersions.

In 2D and 3D inertial-subrange turbulence, two-particle statistics follow Richardson's two classic scaling laws: 1) scale-dependent relative diffusivity  $\mu \sim l^{4/3}$  and 2)  $D^2(t) \sim t^3$  growth rate of the relative dispersion. For classical isotropic inertial-subrange turbulence, Obukhov (1941a,b) and Batchelor (1950) provided the theoretical basis for these scaling laws using dimensional arguments. These scalings have been observed in direct numerical simulations of 2D (Boffetta and Sokolov 2002b) and 3D turbulence (Boffetta and Sokolov 2002a) and in laboratory experiments of 2D turbulence (Jullien et al. 1999).

From the drifter trajectories, the relative dispersion is calculated directly using

$$D_{ii}^2(t, \mathbf{s}_0) = \langle [s_i(t) - s_{0i}]^2 \rangle - \langle [s_i(t) - s_{0i}] \rangle^2, \quad (15)$$

where angle brackets now denote ensemble averaging over all the two-particle trajectories. To reduce the number of dependent variables, increase the amount of data averaged in (15), and simplify the interpretation, the relative dispersion is calculated as a function of initial separation magnitude  $|\mathbf{s}_0|$  rather than  $\mathbf{s}_0$ . Initial  $|\mathbf{s}_0|$  are placed into bins between 0 and 4, 4 and 8, 8 and 16, and 16 and 32 m and greater than 32 m. Furthermore, to increase the amount of data used in (15), for two individual trajectories that overlap in time for 200 s, for example, 199 different (but not independent) two-particle trajectories are used (recall that position is sampled at 1 Hz). To be specific, when  $t = 0$  the initial separation is  $\mathbf{s}_0$  and a 200-s two-particle trajectory  $\mathbf{s}(t)$  is determined. Then for  $t = 1$ ,  $\mathbf{s}_0$  is updated and a different (but not independent) 199-s two-particle trajectory is determined. This is repeated to yield 199 two-particle trajectories, each with a different  $\mathbf{s}_0$ , that are 1–200 s in length. This is repeated for all possible pairs of drifters in a release. At each  $\mathbf{s}_0$ , statistics are only shown for  $t < 300$  s because the data are insufficient to yield reliable statistics. This also precludes examination of the cross-shore dependence of the two-particle statistics. Therefore two-particle statistics are calculated over the entire sampled region.

Similar to ensemble averaged patches, on day 1 the average size of an individual tracer patch is larger in the  $x$  direction ( $D_{xx}^2 > D_{yy}^2$ ) for  $t < 10$  s, and thereafter (for all but the smallest initial sizes) it is larger in the  $y$  direction (Figs. 10a,c). On day 2, the patch is initially almost circular but becomes elongated in the  $y$  direction for  $t > 100$  s (Figs. 10b,d). Both  $D_{xx}^2$  and  $D_{yy}^2$  increase as a power law in  $t$ ,  $D_{ii}^2(t) \sim t^\gamma$ . The average (over  $|\mathbf{s}_0|$ ) exponent of each two-particle dispersion is shown in Figs. 10e,f. On both days,  $\gamma$  first ( $t \leq 10$  s) decreases from about 3 to about 1 and then varies between 1 and

2 (Figs. 10e,f), with values that are larger on day 1 than on day 2, and  $y$  values are typically larger than  $x$  values on both days. The observed power-law scaling is not consistent with inertia-subrange turbulence where  $D^2 \sim t^3$  applies.

The relative diffusivity, as defined in (13), is plotted in Fig. 11 versus  $d$ , where

$$d = [D_{xx}(t, |\mathbf{s}_0|)D_{yy}(t, |\mathbf{s}_0|)]^{1/2} \quad (16)$$

is the radius of a circle with area equal to an ellipses with axes  $D_{xx}$  and  $D_{yy}$ . The spatial growth of a patch after  $t_0$  (and not the overall patch size) is characterized by  $d$ , because the original separation  $\mathbf{s}_0$  is removed from  $D$ . At  $d$  larger than about 4 m (corresponding to  $t > 10$  s), the dependence of  $\mu_{xx}$  and  $\mu_{yy}$  on  $d$  is weaker than Richardson-like (i.e.,  $\lambda < 4/3$  in  $\mu \sim d^\lambda$ ). Using the actual patch size  $l$ , estimated from  $l = (d^2 + |\mathbf{s}_0|^2)^{1/2}$ , rather than  $d$  does not change the power-law dependence of  $\mu$ . In general,  $\mu_{yy}$  depends more strongly on separation than does  $\mu_{xx}$  (Fig. 11). The largest relative diffusivities observed (for the largest initial separations and times) are  $\mu_{xx} = 0.7$  (1.3)  $\text{m}^2 \text{s}^{-1}$  and  $\mu_{yy} = 1.7$  (4)  $\text{m}^2 \text{s}^{-1}$  for day 1 (2).

Although neither inertial-subrange turbulence scaling ( $D^2 \sim t^3$  or  $\mu \sim l^{4/3}$ ) is observed, the two-particle statistics have some similarities with inertial-subrange dispersion. For example,  $D^2$  is larger for larger initial separations (cf. curves in Figs. 10 a–d at fixed  $t$ ) with growth rates greater than  $t$ , and (except for  $\mu_{xx}$  on day 2) the diffusivity is scale-dependent.

The two-particle observations are generally consistent with a diffusion equation for particle separations (Richardson 1926; Kraichnan 1966):

$$\partial_t P_s(s, t) = \kappa_0 \partial_s [s^{2-\alpha} t^{\beta-1} \partial_s P_s(s, t)], \quad (17)$$

where  $P_s$  is the probability of the two particles having separation  $s$  and  $\alpha$  and  $\beta$  are constants. Note the units for  $\kappa_0$  are  $\text{m}^\alpha \text{s}^{-\beta}$  and  $s$  is either the  $x$  or  $y$  separation. The solution of (17) for  $P_s(s, t = 0) = \delta(s)$  is

$$P_s = A \exp(-C|s|^\alpha t^{-\beta}) \quad (18)$$

with

$$C = \frac{\beta}{\alpha^2 \kappa_0} \quad \text{and} \quad A = \frac{\alpha C^{1/\alpha}}{2t^{\beta/\alpha} \Gamma(1/\alpha)}, \quad (19)$$

where  $\Gamma(z)$  is the gamma function. The second moment of  $P_s$  is the relative dispersion

$$D^2(t) = \int s^2 P_s(s, t) ds = \frac{b}{C^{2/\alpha}} t^{2\beta/\alpha}, \quad (20)$$

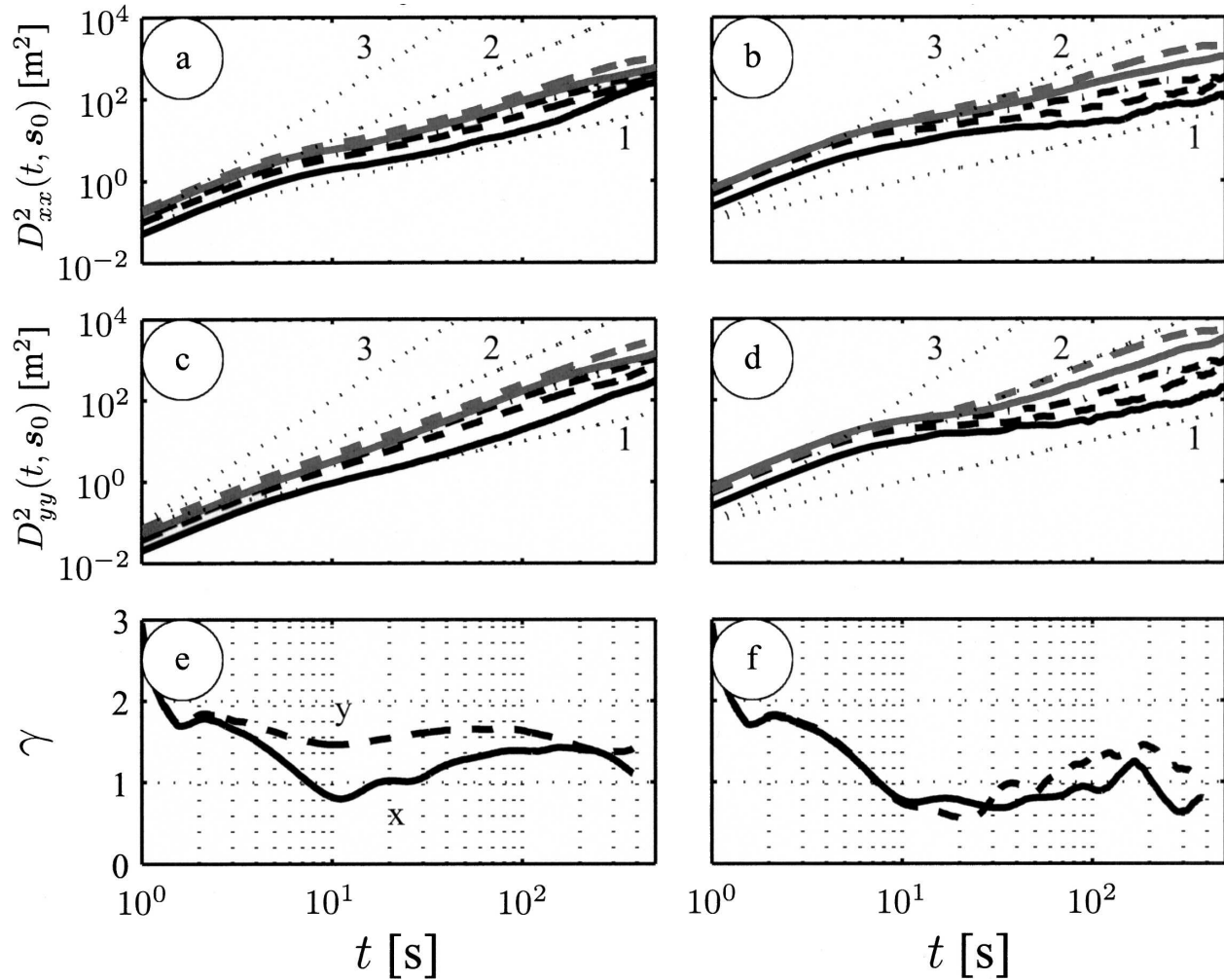


FIG. 10. Two-particle dispersion: (a), (b)  $D^2_{xx}(t)$ , (c), (d)  $D^2_{yy}(t)$ , and (e), (f)  $\gamma$  (where  $D^2 \sim t^\gamma$ ) vs time. For dispersion, the initial separation  $|s_0|$  is indicated by line style and shade:  $<4$  (solid black),  $4\text{--}8$  (dashed black),  $8\text{--}16$  (dashed-dotted black),  $16\text{--}32$  (solid gray), and  $>32$  m (dashed gray). Three different scalings are indicated,  $D^2 \sim t^\gamma$  with  $\gamma = 1, 2,$  and  $3$ , in (a)–(d). In (e), and (f), the dashed line is  $\gamma$  in the  $y$  dispersion ( $D^2_{yy} \sim t^\gamma$ ) and the solid line is  $\gamma$  for  $x$  dispersion.

where  $b = [\Gamma(3/\alpha)]/[\Gamma(1/\alpha)]$ . The diffusivity,

$$\mu = \frac{1}{4} \frac{d}{dt} D^2(t),$$

is

$$\mu(D) = \frac{\beta}{2\alpha} b^{\alpha/2\beta} C^{-1/\beta} D^{2-\alpha/\beta} \quad (21)$$

as a function of  $D$ . Thus, for this diffusion model

$$D^2 \sim t^\gamma \quad \text{with} \quad \gamma = 2\beta/\alpha \quad (22)$$

and

$$\mu \sim D^\lambda \quad \text{with} \quad \lambda = 2 - \alpha/\beta. \quad (23)$$

There is a direct relationship between  $\gamma$  and  $\lambda$ :

$$\gamma = 2/(2 - \lambda). \quad (24)$$

In 2D inertial-subrange turbulence,  $\beta = 1$  and  $\alpha = 2/3$  for  $t$  less than the time it takes two particles to separate a distance similar to the largest turbulent length scales (Richardson 1926), recovering the scaling laws  $D^2 \sim t^3$  and  $\mu \sim D^{4/3}$ . At larger separations, comparable to the largest spatial scales in the flow, the particles move independently and the separation statistics become Gaussian—that is,  $\alpha = 2$  [as found in Boffetta and Sokolov (2002b)].

The pdf of pair separations is now examined. First, a similarity (“normalized”) solution  $\hat{P}$  is generated by defining  $\hat{s} = s/D$  and  $\hat{P} = P_s D$ , resulting in

$$\hat{P}(\hat{s}) = \frac{\alpha}{2\Gamma(1/\alpha)} b^{1/2} \exp(-b^{\alpha/2} |\hat{s}|^\alpha) \quad (25)$$

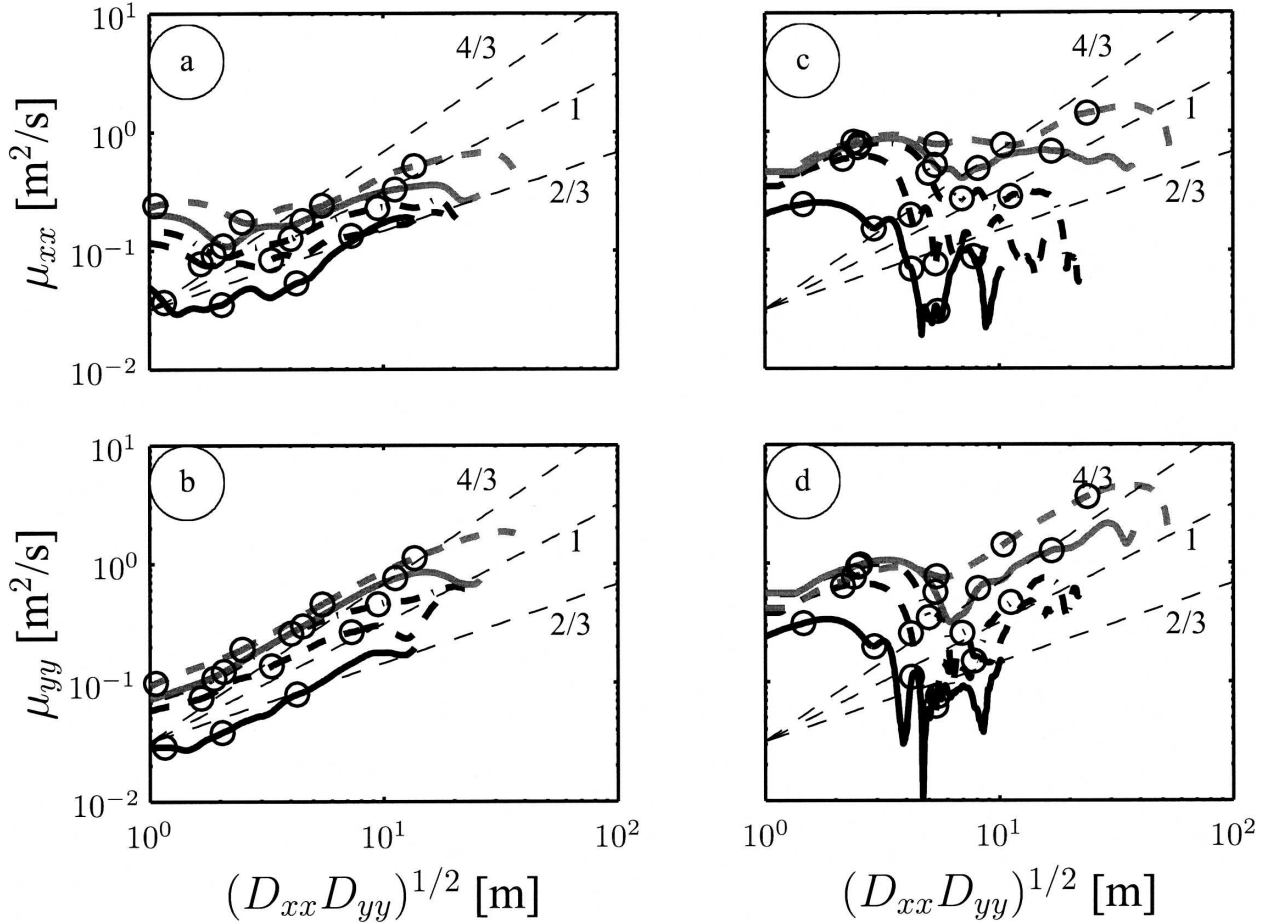


FIG. 11. Two-particle diffusivity  $\mu$  as a function of separation  $d$ : (left) day 1 and (right) day 2. Line shades and styles indicate initial separation (see Fig. 10 for details), and dashed thin lines are power-law scalings:  $\mu \sim d^\lambda$  with  $\lambda = 2/3, 1,$  and  $4/3$ . The open circles indicate times at which  $\log_{10}(t) = 0.5, 1.0, 1.5,$  and  $2$  ( $t = 3, 10, 31,$  and  $100$  s).

eliminating the  $t$  and  $\beta$  dependence in  $P_s$ . Thus,  $\hat{P}(\hat{s})$  depends only on  $\alpha$ . The normalized  $\hat{P}(\hat{s})$  is calculated for  $t$  between 1 and 200 s and  $|s_0| < 4$  m. On both days, the normalization  $\hat{P}(\hat{s})$  collapses the observed  $x$  and  $y$  separations onto a self-similar pdf (Fig. 12), and, for all times,  $\hat{P}$  is more Richardson-like ( $\alpha = 2/3$ ) than Gaussian ( $\alpha = 2$ ). This indicates that after 200 s drifters initially within 4 m of one another have not yet drifted apart sufficiently to move independently. Because the distribution of separations collapses onto a self-similar Richardson-like pdf, (17) with  $\alpha = 2/3$  applies to the observed separations. Results for other  $|s_0|$  are similar and are not shown.

If pair separations evolve according to (17) and one of the scaling laws is known (either  $D^2 \sim t^\gamma$  or  $\mu \sim D^\lambda$ ), the unknown scaling law (and therefore  $\beta$ ) can be determined using (24). The slope of the best-fit line of  $\log(\mu)$  versus  $\log(d)$  (not shown) yields a  $\lambda$  estimate for each initial separation  $s_0$ . The fit is only for values of  $d$  larger than about 4 m, excluding the initial small  $d$

anomalous behavior of  $\mu$  (Fig. 11). The average over all  $s_0$  is denoted  $\langle \lambda \rangle$ . Using  $\langle \lambda \rangle$ , inferred values of  $\gamma$  are found from  $\gamma^{\text{IN}} = 2/(2 - \langle \lambda \rangle)$  (Table 1, column 4). Directly estimating  $\gamma$  from  $D^2 \sim t^\gamma$  (Figs. 10e,f) and averaging values of  $\gamma$  for  $t > 50$  s yields  $\langle \lambda \rangle$  (Table 1, column 5). On both days, and in both  $x$  and  $y$ , there is rough correspondence between the directly estimated ( $\langle \lambda \rangle$ ) and the inferred ( $\gamma^{\text{IN}}$ ) values. For example, on each day, both  $\gamma$  estimates have larger  $y$  components than  $x$  components.

The observed drifter separations are due neither to independent motions nor to inertial-subrange turbulence. However, the correspondence between  $\langle \lambda \rangle$  and  $\gamma^{\text{IN}}$  and the shape of the self-similar pdfs suggest the separations are consistent with (17) using  $\alpha = 2/3$  and  $\beta = 1/2$  corresponding to the scaling laws  $D^2 \sim t^{3/2}$  and  $\mu \sim l^{2/3}$  (the average value of  $\gamma^{\text{IN}}$  in column 4 of Table 1 is 1.44). Because data from both days and directions are included in this estimate, these scaling laws are representative of the entire dataset. However, scaling laws

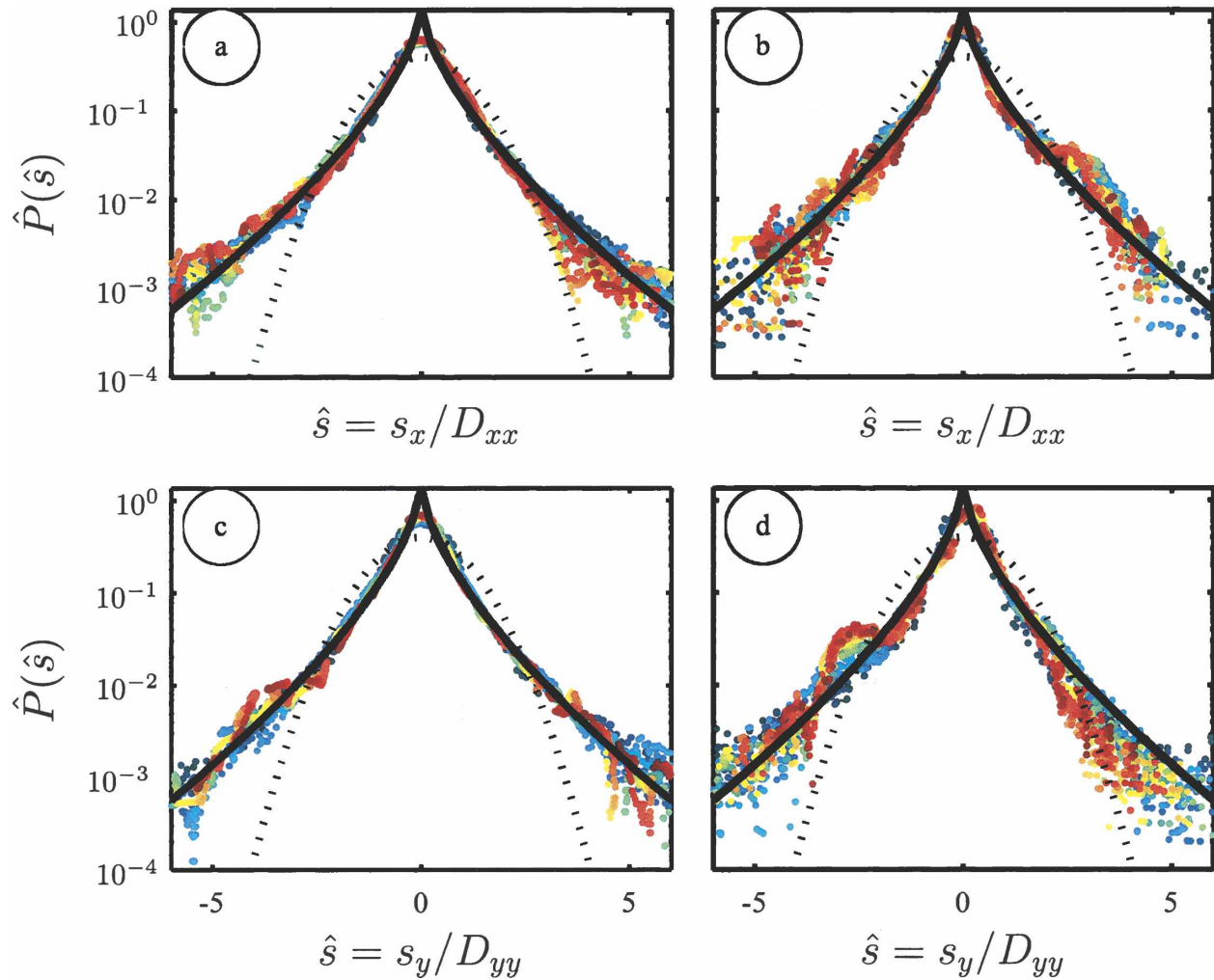


FIG. 12. Two-particle self-similar pdf  $\hat{P}$  [(25)] as a function of separation  $\hat{s}$ . The Richardson [ $\alpha = 2/3$  so  $\hat{P} \sim \exp(-b^{1/3}|\hat{s}|^{2/3})$ ; solid line] and Gaussian [ $\alpha = 2$  so  $\hat{P} \sim \exp(-b|\hat{s}|^2)$ ; dotted line] pdfs are shown for reference. Time is indicated by color:  $t = 0$  s is blue,  $t = 200$  s is red, and other colors are intermediate times.

for each day and direction can be determined from Table 1. The constant  $\kappa_0$ , from (20), is

$$\kappa_0 = \frac{\beta}{\alpha^2} \left[ \frac{D^2(t)}{bt^{2\beta/\alpha}} \right]^{\alpha/2}. \quad (26)$$

Estimates of  $\kappa_0$  in Table 1, for each day and direction, are determined from (26) averaged between 100 and 200 s with  $\alpha = 2/3$ ,  $\beta = 1/2$ , and  $|\mathbf{s}_0| < 4$  m [eliminating the effect of the original separation on  $D^2(t)$ ]. Direct comparison of  $\kappa_0$  between days is not possible because the  $\kappa_0$  have different units.

TABLE 1. Table of dispersion scaling-law exponents. The dispersion scales like  $D^2(t) \sim t^\gamma$ , and the diffusion scales like  $\mu \sim d^\lambda$ . The inferred  $\gamma^{\text{IN}}$  [ $=2/(2 - \langle\lambda\rangle)$ ] and directly estimated  $\langle\gamma\rangle$  are shown with standard error estimates. Also calculated is an estimate of the constant  $\kappa_0$ .

Day	Direction	$\langle\lambda\rangle$	$\gamma^{\text{IN}}$	$\langle\gamma\rangle$	$\kappa_0$ ( $\text{m}^\alpha \text{s}^{-\beta}$ )
1	x	0.64 ( $\pm 0.01$ )	1.47 ( $\pm 0.01$ )	1.35 ( $\pm 0.09$ )	0.14
1	y	0.83 ( $\pm 0.01$ )	1.71 ( $\pm 0.02$ )	1.53 ( $\pm 0.11$ )	0.13
2	x	-0.31 ( $\pm 0.01$ )	0.87 ( $\pm 0.01$ )	0.90 ( $\pm 0.18$ )	0.21
2	y	0.84 ( $\pm 0.02$ )	1.72 ( $\pm 0.02$ )	1.24 ( $\pm 0.12$ )	0.18

## 5. Discussion

### a. Comparison with other diffusivity estimates

Johnson and Pattiaratchi (2004) used the spreading rate of multiple drifters to estimate scale-dependent relative diffusivities in the surf zone. For approximately 10–50-m separations,  $1.3 < \mu < 3.9 \text{ m}^2 \text{ s}^{-1}$  with  $\mu_{yy} > \mu_{xx}$ . These diffusivities are based on individual realizations rather than ensemble averages used here. For 10–50-m separations, our results for  $\mu$  are similar,  $0.1 < \mu < 1.0$ , although for the largest separations on day 2,  $\mu_{yy} \approx 4 \text{ m}^2 \text{ s}^{-1}$  (Fig. 11d). Both this beach and that in Johnson and Pattiaratchi (2004) lacked a pronounced bar and had similar slopes. However, rip currents were not present here, whereas in Johnson and Pattiaratchi (2004) they were the dominant circulation feature contributing significantly to  $\mu$ . For much larger dye-patch sizes,  $O(10^2\text{--}10^3) \text{ m}$ , Grant et al. (2005) report much larger surf-zone alongshore diffusivities with  $40 < \mu_{yy} < 80 \text{ m}^2 \text{ s}^{-1}$ . These values, and the two-particle statistics obtained here, suggest a scale-dependent relative diffusivity.

Many prior surf-zone diffusivity estimates used observations of dye concentration to calculate  $\kappa^\infty$  in variants of (1). Early investigators found  $0.08 < \kappa_{xx} < 5.9 \text{ m}^2 \text{ s}^{-1}$  and  $0.03 < \kappa_{yy} < 0.17 \text{ m}^2 \text{ s}^{-1}$  (Inman et al. 1971), and Clarke et al. (2007) report values  $O(10^{-1}\text{--}10^2) \text{ m}^2 \text{ s}^{-1}$  depending on the diffusion model and diffusivity component. These  $\kappa$  values are based on single realizations rather than ensemble averages, and Clarke et al. (2007) noted that different portions of their concentration time series were better fit by variable  $\kappa$ . Despite these differences, our estimates of  $\kappa$ ,  $\kappa_{xx}^\infty = 0.7 (1.5) \text{ m}^2 \text{ s}^{-1}$  and  $\kappa_{yy}^\infty = 2 (4.5) \text{ m}^2 \text{ s}^{-1}$  on day 1 (2) (Figs. 7, 8), are within the range, although on the large side of previously reported dye-based values.

The drifters used in this work [and in Johnson and Pattiaratchi (2004)] are designed not to surf shoreward, and therefore the dispersive effect of breaking waves and bores is minimized. On the other hand, dye is spread shoreward by broken waves. The relationship between dye-based and drifter-based estimates of surf-zone dispersion is unclear. Other difficulties inherent in using drifters to measure surf-zone dispersion include strong cross-shore-dependent and nonstationary statistics, the effect of which is unknown. Furthermore, one- and two-particle statistics have been obtained for only a small range of waves, circulations, and beach morphologies, and therefore the effect of different environmental conditions (e.g., wave height, circulation, and bottom slope) on dispersion is not understood.

### b. Mechanisms of dispersal

Two-particle separations suggests a self-similar turbulent regime similar to a 2D inertial subrange (Jullien et al. 1999; Boffetta and Sokolov 2002b). Physical processes responsible for the observed one- and two-particle dispersion examined below include surface gravity waves (both sea swell and infragravity waves), shear waves (day 2), shear dispersion (day 2), and vorticity induced by alongshore gradients in breaking-wave heights.

#### 1) SURFACE GRAVITY WAVES

Although not classically turbulent (i.e., rotational), the fluctuations of Stokes drift in a random, irrotational, weakly nonlinear surface gravity wave field also cause dispersion (Herterich and Hasselmann 1982). On both days,  $\kappa_{xx}$  rapidly grows for time lags  $t < 10 \text{ s}$  (e.g., Figs. 7a, 8a) because the Lagrangian velocity covariance  $C_{uu}$  is largest at these time lags, suggesting that surface gravity waves could be a major contributor to the observed one-particle dispersion.

For any weakly nonlinear waves, the one- and two-particle diffusivities can be calculated from wavenumber spectrum and the dispersion relationship (Balk 2002). For deep-water surface gravity waves, Herterich and Hasselmann (1982) developed expressions for the asymptotic one-particle diffusivity  $\kappa^\infty$ . This can be straightforwardly extended into shallow water, and assuming only  $+x$  propagating waves, results in the asymptotic wave-induced diffusivity

$$\kappa_{xx}^{\text{HH}} = \pi \frac{g}{h^3} \int_0^\infty S_\eta^2(\omega) d\omega, \quad (27)$$

where  $S_\eta(\omega)$  is the sea surface height frequency spectrum ( $\omega$  is the radian frequency),  $h$  is the shallow water depth, and  $g$  is gravity. From the ADV measurements this diffusivity is calculated over frequencies  $0.004 < f < 0.3 \text{ Hz}$  including infragravity and sea-swell contributions. Infragravity contributions to (27) are small relative to the sea swell. All energy is assumed to be shoreward propagating; thus, the  $\kappa_{xx}^{\text{HH}}$  estimates are upper bounds.

On day 1 the maximum wave-induced diffusivity  $\kappa_{xx}^{\text{HH}} = 0.003 \text{ m}^2 \text{ s}^{-1}$  at the innermost ADV, and on day 2 the maximum  $\kappa_{xx}^{\text{HH}} = 0.023 \text{ m}^2 \text{ s}^{-1}$  at the middle ADV. Because these  $\kappa_{xx}^{\text{HH}}$  estimates are two orders of magnitude smaller than observed (Figs. 7a,b and 8a,b), random Stokes drift dispersion, based on irrotational flow, cannot explain the observed drifter dispersion. The assumption of weak nonlinearity required in (27) may be violated in the surf zone, but this error seems unlikely to increase the wave-induced diffusivity by orders of magnitude.

## 2) SHEAR DISPERSION

Sheared mean currents can enhance diffusivities in the flow direction—an effect known as shear dispersion. Although the weak currents on day 1 preclude significant shear dispersion, modest shear in the along-shore current  $\bar{v}$  on day 2 (Fig. 4c) may contribute to the effective  $\kappa_{yy}$ . Following the Taylor (1953) analysis of

shear dispersion in pipes, a parabolic representation of  $\bar{v}(x)$  is chosen for simplicity and analytic tractability:  $\bar{v}(x) = v_0(x/L_x)(1 - x/L_x)$ . With drifters initially distributed uniformly on a cross-shore line,  $C(x, y, t) = \delta(y)\delta(t)$ , the mean drifter alongshore location  $\bar{y} = \langle yC(x, y, t) \rangle$  (angle brackets denote integration over all space) is  $\bar{y} = 2v_0t/3$  for all times. The alongshore variance of drifter positions has three regimes:

$$\overline{(y - \bar{y})^2} = \langle (y - \bar{y})^2 C(x, y, t) \rangle \approx \begin{cases} 2\kappa_{yy}t, & t < \frac{45}{2} \kappa_{yy}/v_0^2 \\ \frac{4}{45} v_0^2 t^2, & \frac{45}{2} \kappa_{yy}/v_0^2 < t < \frac{3}{64} L_x^2/\kappa_{xx} \\ 2\kappa_{se}t, & t > \frac{3}{64} L_x^2/\kappa_{xx} \end{cases} \quad (28)$$

with the long-time shear-enhanced diffusivity given by

$$\kappa_{se} = \frac{L_x^2 v_0^2}{480 \kappa_{xx}}. \quad (29)$$

The first regime,  $t < 45\kappa_{yy}/2v_0^2$ , is due to random along-shore motions, because the elapsed time is not long enough for  $\bar{v}(x)$  to curve the drifter line. Furthermore, this is the only regime if  $\kappa_{yy} > L_x^2 v_0^2 / (480 \kappa_{xx})$ . In the second “advection” regime, the drifter line is curved by  $\bar{v}(x)$  and the variance grows like  $t^2$  and thus the diffusivity grows like  $t$ . The long-time regime occurs when cross-shore diffusion allows drifters to sample the entire current.

Fitting a parabola to the alongshore average of  $\bar{v}$  on day 2 (Fig. 4c) results in  $v_0 = -0.53 \text{ m s}^{-1}$  and  $L_x = -170 \text{ m}$ . In the advection regime, the shear-dispersion-induced diffusivity is given by  $d\overline{(y - \bar{y})^2}/2dt = 4v_0^2 t/45 \approx 0.023t$ . The observed  $\kappa_{yy}$  grows approximately linearly in time for  $20 < t < 200 \text{ s}$  with slope  $d\kappa_{yy}/dt \approx 0.025$  (Fig. 8d). This agreement suggests that the observed growth of  $\kappa_{yy}(t)$  during this time could result from advection. However, on day 2 the observed  $\kappa_{yy}$  reaches an asymptotic value when  $t \approx 200 \text{ s}$ , whereas for the shear dispersion model this time corresponds to  $\kappa_{xx} = 3L_x^2/(64 \times 200 \text{ s}) \approx 6.8 \text{ m}^2 \text{ s}^{-1}$ , roughly 5 times that observed. At long times, the observed  $\kappa_{xx} = 1.5 \text{ m}^2 \text{ s}^{-1}$  yields  $\kappa_{se} = 11.3 \text{ m}^2 \text{ s}^{-1}$  for  $t > 903 \text{ s}$ . Thus, using the observed  $\kappa_{xx}$  in this model overpredicts both the asymptotic diffusivity (by roughly a factor of 3) and the time to asymptotic approach. However, all long-time estimates are qualitative for three reasons: 1) lack of long ( $t > 1000 \text{ s}$ ) drifter trajectories, 2) rapidly growing er-

rors in the observed  $\kappa_{ij}$  (appendix B), and 3) use of biased Lagrangian velocity autocovariance functions (biased toward zero at long times) to compute  $\kappa_{ij}$ . Note that the diffusivity is scale-independent in this simple shear dispersion model, and therefore the particle pair separations are Gaussian rather than Richardson-like as observed (Fig. 12).

## 3) SURF-ZONE VORTICITY

Aspects of two-particle separation statistics suggest that 2D turbulence with a wide range of eddy scales is causing the surf-zone dispersion. For example, the normalized separation pdfs (Fig. 12) resemble those in 2D inertial-subrange turbulence (Jullien et al. 1999). However, the time dependence of the relative dispersion and the diffusivity’s scale dependence differ from 2D inertial-subrange scalings (Batchelor 1950). Thus, the 2D surf-zone eddy field responsible for dispersion is not a classical 2D inertial subrange (an energy cascade; see Salmon 1998); rather it is inertial-subrangeline: that is, a vorticity-dominated eddy field with length scales 5–50 m (Fig. 11). Furthermore, the cross-shore depth variation may also be important to the 2D surf-zone eddy field.

The source of this vorticity is not understood. Shear waves likely were not present on day 1, and on day 2 they would input vorticity at length scales  $O(10^2) \text{ m}$  (e.g., Oltman-Shay et al. 1989), which, for flat-bottom 2D turbulence, would cascade energy to larger length scales—too large to explain the observed 5–50-m scale-dependent diffusivities. Shear waves may be important for dispersion at large length scales; however, data at such scales are lacking on day 2.

We speculate that the source of vorticity (eddies) with scales less than about 50 m is alongshore gradients in breaking-wave heights (Peregrine 1998) associated with finite crest length. Theory and numerical simulations (Peregrine 1998; Bühler and Jacobson 2001) show that alongshore gradients in bore dissipation can create vertical vorticity on 5–50-m length scales. In addition, Boussinesq model surf-zone circulation simulations, which implicitly include this vorticity generation mechanism, reveal a rich eddy field with vorticity at a range of scales (Chen et al. 2003). This mechanism, linked to wave breaking, applies to both days and provides the range of length scales required for the observed scale-dependent diffusivity (Fig. 11).

## 6. Summary

Surf-zone dispersion is quantified using one- and two-particle statistics derived from Lagrangian drifter data acquired on two days with contrasting waves and currents. On day 1, approximately normally incident waves were relatively small ( $H_s \approx 0.5$  m) and currents were weak ( $|\bar{v}| < 0.1$  m s<sup>-1</sup>). On day 2, waves were obliquely incident and larger ( $H_s \approx 1.4$  m), driving a current that reached  $|\bar{v}| \approx 0.7$  m s<sup>-1</sup> in the surf zone.

Larger waves and stronger alongshore currents correspond to larger diffusivities. On day 2, diffusivities (both one and two particle) were approximately 2 times those on day 1. On both days, the one-particle diffusivities are time-dependent. The strongest diffusion is initially in the cross-shore ( $x$ ) direction; after many wave periods, however, the one-particle diffusivity in the alongshore ( $y$ ) direction was approximately 2 times that in  $x$ . Thus, at long times an ensemble-averaged surf-zone tracer spreads more quickly in  $y$  than in  $x$ . The asymptotic values of the diffusivity are  $\kappa_{xx}^\infty = 0.7$  (1.5) m<sup>2</sup> s<sup>-1</sup> and  $\kappa_{yy}^\infty = 2$  (4.5) m<sup>2</sup> s<sup>-1</sup> on day 1 (2). The asymptotic values of the one-particle diffusivity (both  $\kappa_{xx}$  and  $\kappa_{yy}$ ) are similar within and seaward of the surf zone; however, asymptotic values are reached faster within the surf zone.

Surf-zone two-particle statistics suggest the presence of inertial-subrangeline turbulence. The form of the two-particle normalized separation probability density functions at all times is nearly identical to those found in 2D inertial-subrange turbulence. Thus, even at the largest times ( $\sim 200$  s) and separations ( $\sim 60$  m), pairs of drifters do not move independently. Two-particle dispersion grows like  $D^2 \sim t^{3/2}$  with scale-dependent relative diffusivity  $\mu \sim t^{2/3}$ . Both scalings differ from classical inertial-subrange turbulence ( $D^2 \sim t^3$  and  $\mu \sim t^{4/3}$ ). Two-particle statistics in the surf zone are consistent with a diffusion equation for the particle separation

pdf in which the diffusivity is both time- and separation-dependent, in contrast to inertial-subrange turbulence in which the diffusivity depends only on separation.

Mechanisms of dispersion were investigated. The theoretical asymptotic diffusivity from the Stokes drift of unbroken irrotational surface gravity waves (sea swell and infragravity waves) is much smaller than observed, suggesting rotational motions are important to surf-zone dispersion. The sheared mean alongshore current observed on day 2 was used in a simple model of shear dispersion. The model overpredicts the one-particle asymptotic diffusivity  $\kappa_{yy}^\infty$  and the time to reach this value. The model does, however, predict the slope of the observed  $t$  growth of  $k_{yy}$  for intermediate times. Although possibly important on day 2, shear dispersion cannot explain day-1 results when  $\bar{v}$  is small. We speculate that a modified two-dimensional turbulent eddy field governs surf-zone dispersion, and the source of this vorticity [at  $O(5\text{--}50)$  m] is alongshore gradients in breaking-wave height associated with finite crest lengths (Peregrine 1998).

*Acknowledgments.* This research was supported in part by California Sea Grant, ONR, and NSF. Sea Grant support was through the National Sea Grant College Program of the U.S. Department of Commerce's National Oceanic and Atmospheric Administration under NOAA Grant NA04OAR4170038, Project 01-C-N, through the California Sea Grant College Program and the California State Resources Agency. The views expressed herein do not necessarily reflect the views of any of those organizations. Staff from the Integrative Oceanography Division of SIO (B. Woodward, B. Boyd, K. Millikan, D. Darnell, and K. Smith) designed and built the drifters and were instrumental in acquiring the field observations. SIO volunteers D. McNamara, A. Ponte, M. Yates, S. Henderson, J. Klymak, S. Johnston, S. Elipot, Y. Lenn, and E. Douglass assisted with the drifter deployments. We give our thanks to all of these people and organizations.

## APPENDIX A

### Degrees of Freedom

The number of independent samples  $N_e$  (Fig. 4) is calculated using a slight modification of the estimator in Bendat and Piersol (2000):

$$N_e/N = (\sigma_u^2 + \sigma_v^2) \left\{ 2 \int_0^\infty [C_{xx}(t) + C_{yy}(t)] dt \right\}^{-1}, \quad (\text{A1})$$

where  $C_{ii}$  is the autocovariance function for the  $i$ th component of velocity,  $N$  is the duration (in seconds) of drifter observations in a bin, and  $\sigma$  is the velocity variance. Thus,  $N_e$  is approximated as the sampling time divided by the total (combining  $u$  and  $v$ ) Lagrangian decorrelation time, and it provides a single representative value of the number of independent data points.

## APPENDIX B

### Diffusivity Sampling Error

Even small sampling errors in  $C_{ij}(t)$  can lead to significant sampling error in  $k_{ij}(t)$ . The present derivation of the  $\kappa(t)$  sampling error follows the derivation of the  $C_{ij}(t)$  sampling error found in Bendat and Piersol (2000). The sampling error is defined as

$$\epsilon_{ij}^2(t) = \text{Var}[\kappa_{ij}(t)] = E\{[\kappa_{ij}(t) - \bar{\kappa}_{ij}(t)]^2\}, \quad (\text{B1})$$

where  $E$  is the expectation operator and the expected value is denoted with an overbar. Expanding the square and taking expectations, we find

$$E\{[\kappa_{ij}(t) - \bar{\kappa}_{ij}(t)]^2\} = E[\kappa_{ij}^2(t)] - \bar{\kappa}_{ij}^2(t). \quad (\text{B2})$$

From the definition of  $\kappa_{ij}(t)$  from (5),

$$E[\kappa_{ij}^2(t)] = E\left[\int_{-t}^0 C_{ij}(t_1) dt_1 \int_{-t}^0 C_{ij}(t_2) dt_2\right]. \quad (\text{B3})$$

After substitution of the definition of the Lagrangian velocity autocovariance into the previous equation,

$$E[\kappa_{ij}^2(t)] = \frac{1}{T_R^2} \int_{-t}^0 \int_{-t}^0 \int_0^{T_R} \int_0^{T_R} E[u_i(a)u_j(a+t_1) \times u_i(b)u_j(b+t_2)] da db dt_2 dt_1, \quad (\text{B4})$$

where  $T_R$  is the drifter record length. Assuming the velocities are all jointly Gaussian random variables and symmetric autocovariance functions gives

$$E[u_i(a)u_j(a+t_1)u_i(b)u_j(b+t_2)] = C_{ij}(t_1)C_{ij}(t_2) + C_{ij}(a-b)C_{ij}(a+t_1-b-t_2) + C_{ij}(a-b-t_2)C_{ij}(a-b+t_1), \quad (\text{B5})$$

and results in

$$E[\kappa_{ij}^2(t)] = \bar{\kappa}_{ij}^2(t) + \frac{1}{T_R^2} \int_{-t}^0 \int_{-t}^0 \int_0^{T_R} \int_0^{T_R} [C_{ii}(a-b) \times C_{ij}(a+t_1-b-t_2) + C_{ij}(a-b-t_2) \times C_{ji}(a-b+t_1)] da db dt_2 dt_1, \quad (\text{B6})$$

with  $\epsilon_{ij}^2(t)$  being the second term on the rhs. Changing the variables of integration as

$$a - b \rightarrow \eta, \quad b \rightarrow b, \quad t_1 - t_2 \rightarrow \zeta, \quad \text{and} \quad t_2 \rightarrow t_2 \quad (\text{B7})$$

leads to

$$\epsilon_{ij}^2(t) = \frac{t}{T_R} \int_{-t}^t \int_{-T_R}^{T_R} \left(1 - \frac{|\eta|}{T_R}\right) \left(1 - \frac{|\zeta|}{t}\right) C_{ii}(\eta) \times C_{jj}(\eta + \zeta) d\eta d\zeta + \frac{1}{T_R} \int_{-t}^0 \int_{-t}^0 \int_{-T_R}^{T_R} \left(1 - \frac{|\eta|}{T_R}\right) \times C_{ij}(\eta - t_2) C_{ji}(\eta + t_1) d\eta d\zeta dt_2, \quad (\text{B8})$$

with only the  $\eta$  and  $b$  variable changes used in the second integral. For  $T_R \gg 1$  and  $t \gg 1$ , the asymptotic limit of  $T_R \gg t$ , for Gaussian autocovariance functions of equal magnitude, is

$$\epsilon_{ij}^2(t) \sim K_1 \frac{t}{T_R} + K_2 \frac{\tau}{T_R}, \quad (\text{B9})$$

with  $K_1 = 4\kappa_{ii}^\infty \kappa_{jj}^\infty$  and  $K_2 = K_1(2\pi)^{1/2}$ . Therefore, (5) is a consistent estimator of  $\kappa(t)$  because  $\epsilon \rightarrow 0$  as  $T_R \rightarrow \infty$ . Estimates of  $\epsilon_{ij}(t)$  are determined by numerically integrating only the first integral in (B8) because it dominates the error for  $t \gg \tau_{ij}$ . Thus, after  $\kappa(t)$  has reached  $\kappa^\infty$ , the rms error in estimating  $\kappa$  grows like  $t^{1/2}$ . Biased  $C_{ij}$  estimates from the drifter velocities are used in the integral. The above estimate of the sampling error assumes that  $C_{ij}$  is determined from a single realization (or time series), whereas we calculate  $C_{ij}$  from  $N_d$  (77 and 63 for days 1 and 2, respectively) almost completely independent drifter trajectories on that day; therefore, dividing  $\epsilon_{ij}^2(t)$  by  $N_d$  results in roughly the correct sampling error in estimating  $\kappa(t)$ . Note that the first term in (B9) was calculated in Davis (1991) and has been used to estimate  $\kappa(t)$  errors in the literature (e.g., Swenson and Niiler 1996).

## REFERENCES

- Balk, A. M., 2002: Anomalous behaviour of a passive tracer in wave turbulence. *J. Fluid Mech.*, **467**, 163–203.
- Batchelor, G. K., 1950: The application of the similarity theory of turbulence to atmospheric diffusion. *Quart. J. Roy. Meteor. Soc.*, **76**, 133–146.
- Bendat, J. S., and A. G. Piersol, 2000: *Random Data, Analysis and Measurement Procedures*. Wiley Interscience, 594 pp.
- Boehm, A. B., S. B. Grant, J. H. Kim, C. D. McGee, S. Mowbray, C. Clark, D. Foley, and D. Wellmann, 2002: Decadal and shorter period variability of surfzone water quality at Huntington Beach, California. *Environ. Sci. Technol.*, **36**, 3885–3892.
- Boffetta, G., and I. M. Sokolov, 2002a: Relative dispersion in fully developed turbulence: The Richardson's law and inter-

- mittency corrections. *Phys. Rev. Lett.*, **88**, doi:10.1103/PhysRevLett.88.094501.
- , and —, 2002b: Statistics of two-particle dispersion in two-dimensional turbulence. *Phys. Fluids*, **14**, 3224–3232.
- Bühler, O., and T. E. Jacobson, 2001: Wave-driven currents and vortex dynamics on barred beaches. *J. Fluid Mech.*, **449**, 313–339.
- Chen, Q., J. T. Kirby, R. A. Dalrymple, F. Shi, and E. B. Thornton, 2003: Boussinesq modeling of longshore currents. *J. Geophys. Res.*, **108**, 3362, doi:10.1029/2002JC001308.
- Clarke, L. B., D. Ackerman, and J. Largier, 2007: Dye dispersion in the surf zone: Measurements and simple models. *Cont. Shelf Res.*, **27**, 650–669.
- Davis, R. E., 1985: Drifter observation of coastal surface currents during CODE: The statistical and dynamical views. *J. Geophys. Res.*, **90**, 4756–4772.
- , 1987: Modeling eddy transport of passive tracers. *J. Mar. Res.*, **45**, 635–665.
- , 1991: Observing the general circulation with floats. *Deep-Sea Res.*, **38**, S531–S571.
- Dever, E. P., M. C. Hendershott, and C. D. Winant, 1998: Statistical aspects of surface drifter observations of circulation in the Santa Barbara Channel. *J. Geophys. Res.*, **103**, 24 781–24 797.
- Doutt, J. D., G. V. Frisk, and H. Martell, 1998: Using GPS at sea to determine the range between a moving ship and a drifting buoy to centimeter-level accuracy. *Proc. Oceans '98*, Nice, France, Institute of Electrical and Electronic Engineering, 1344–1347.
- Einstein, A., 1956: *Investigations on the Theory of the Brownian Movement*. Dover, 122 pp.
- Ferrari, R., and R. A. Plumb, 2003: The residual circulation in the ocean. *Near-Boundary Processes and Their Parameterization: Proc. 'Aha Huliko'a Hawaiian Winter Workshop*, Honolulu, HI, University of Hawaii at Manoa, 219–228.
- George, R., and J. L. Largier, 1996: Description and performance of finescale drifters for coastal and estuarine studies. *J. Atmos. Oceanic Technol.*, **13**, 1322–1326.
- Grant, S. B., J. H. Kim, B. H. Jones, S. A. Jenkins, J. Wasyl, and C. Cudaback, 2005: Surf zone entrainment, along-shore transport, and human health implications of pollution from tidal outlets. *J. Geophys. Res.*, **110**, C10025, doi:10.1029/2004JC002401.
- Haile, R. W., and Coauthors, 1999: The health effects of swimming in ocean water contaminated by storm drain runoff. *Epidemiology*, **10**, 355–363.
- Herterich, K., and K. Hasselmann, 1982: The horizontal diffusion of tracers by surface waves. *J. Phys. Oceanogr.*, **12**, 704–711.
- Inman, D. L., R. J. Tait, and C. E. Nordstrom, 1971: Mixing in the surfzone. *J. Geophys. Res.*, **26**, 3493–3514.
- Jiang, S. C., and W. Chu, 2004: PCR detection of pathogenic viruses in southern California urban rivers. *J. Appl. Microbiol.*, **97**, 17–28.
- Johnson, D., and C. Pattiaratchi, 2004: Transient rip currents and nearshore circulation on a swell-dominated beach. *J. Geophys. Res.*, **109**, C02026, doi:10.1029/2003JC001798.
- Jullien, M.-C., J. Paret, and P. Tabeling, 1999: Richardson pair dispersion in two-dimensional turbulence. *Phys. Rev. Lett.*, **82**, 2872–2875.
- Kraichnan, R. H., 1966: Dispersion of particle pairs in homogeneous turbulence. *Phys. Fluids*, **9**, 1937–1943.
- LaCasce, J. H., and A. Bower, 2000: Relative dispersion in the subsurface North Atlantic. *J. Mar. Res.*, **58**, 863–894.
- Lumpkin, R., A. Treguier, and K. Speer, 2002: Lagrangian eddy scales in the northern Atlantic Ocean. *J. Phys. Oceanogr.*, **32**, 2425–2440.
- Obukhov, A. M., 1941a: Spectral energy distribution in a turbulent flow. *Kokl. Akad. Nauk SSSR*, **32**, 22–24.
- , 1941b: Spectral energy distribution in a turbulent flow. *Izv. Akad. Nauk SSSR Ser. Khim.*, **5**, 453–466.
- Okubo, A., 1971: Oceanic diffusion diagrams. *Deep-Sea Res.*, **18**, 789–802.
- Oltman-Shay, J., P. A. Howd, and W. A. Birkemeier, 1989: Shear instabilities of the mean longshore current 2. Field observations. *J. Geophys. Res.*, **94**, 18 031–18 042.
- Peregrine, D. H., 1998: Surf zone currents. *Theor. Comput. Fluid Dyn.*, **10**, 295–309.
- Plumb, R. A., 1979: Eddy fluxes of conserved quantities by small-amplitude waves. *J. Atmos. Sci.*, **36**, 1699–1704.
- Reeves, R. L., S. B. Grant, R. D. Mrse, C. M. C. Oancea, B. F. Sanders, and A. B. Boehm, 2004: Scaling and management of fecal indicator bacteria in runoff from a coastal urban watershed in southern California. *Environ. Sci. Technol.*, **38**, 2637–2648.
- Richardson, L. F., 1926: Atmospheric diffusion shown on a distance-neighbour graph. *Proc. Roy. Soc. London A*, **110**, 709–737.
- Ruessink, B. G., J. R. Miles, F. Feddersen, R. T. Guza, and S. Elgar, 2001: Modeling the alongshore current on barred beaches. *J. Geophys. Res.*, **106**, 22 451–22 463.
- Salmon, R., 1998: *Lectures on Geophysical Fluid Dynamics*. Oxford University Press, 378 pp.
- Schiff, K. C., M. J. Allen, E. Y. Zeng, and S. M. Bay, 2000: Southern California. *Mar. Pollut. Bull.*, **41**, 76–93.
- Schmidt, W. E., B. T. Woodward, K. S. Millikan, and R. T. Guza, 2003: A GPS-tracked surf zone drifter. *J. Atmos. Oceanic Technol.*, **20**, 1069–1075.
- , R. T. Guza, and D. N. Slinn, 2005: Surf zone currents over irregular bathymetry: Drifter observations and numerical simulations. *J. Geophys. Res.*, **110**, C12015, doi:10.1029/2004JC002421.
- Swenson, M. S., and P. P. Niiler, 1996: Statistical analysis of the surface circulation of the California Current. *J. Geophys. Res.*, **101**, 22 631–22 646.
- Taylor, G. I., 1921: Diffusion by continuous movements. *Proc. London Math. Soc.*, **20**, 196–212.
- , 1953: Dispersion of soluble matter in solvent flowing slowly through a tube. *Proc. Roy. Soc. London A*, **219**, 186–203.
- Zhurbas, V., and I. S. Oh, 2003: Lateral diffusivity and Lagrangian scales in the Pacific Ocean as derived from drifter data. *J. Geophys. Res.*, **108**, 3141, doi:10.1029/2002JC001596.